



Spreading rate, spreading obliquity, and melt supply at the ultraslow spreading Southwest Indian Ridge

Mathilde Cannat

Equipe de Géosciences Marines, CNRS-UMR 7154, Institut de Physique du Globe, 4 Place Jussieu, F-75252 Paris Cédex 05, France (cannat@ipgp.jussieu.fr)

Daniel Sauter

Institut de Physique du Globe de Strasbourg, CNRS-UMR 7516, 5 Rue Descartes, F-67084 Strasbourg Cédex, France

Antoine Bezos

Laboratoire de Planétologie et Géodynamique de Nantes, CNRS-UMR 6112, Université de Nantes, 2 Rue de la Houssinière, BP 92208, F-44322 Nantes Cédex 3, France

Christine Meyzen

Laboratoire des Sciences de la Terre, CNRS-UMR 5570, Ecole Nationale Supérieure de Lyon, Université Claude Bernard Lyon 1, 46 Allée d'Italie, F-69364 Lyon Cédex 07, France (christine.meyzen@ens-lyon.fr)

Eric Humler

Laboratoire de Planétologie et Géodynamique de Nantes, CNRS-UMR 6112, Université de Nantes, 2 Rue de la Houssinière, BP 92208, F-44322 Nantes Cédex 3, France

Marion Le Rigoleur

Equipe de Géosciences Marines, CNRS-UMR 7154, Institut de Physique du Globe, 4 Place Jussieu, F-75252 Paris Cédex 05, France

[1] We use bathymetry, gravimetry, and basalt composition to examine the relationship between spreading rate, spreading obliquity, and the melt supply at the ultraslow spreading Southwest Indian Ridge (SWIR). We find that at regional scales (more than 200 km), melt supply reflects variations in mantle melting that are primarily controlled by large-scale heterogeneities in mantle temperature and/or composition. Focusing on adjacent SWIR regions with contrasted obliquity, we find that the effect of obliquity on melt production is significant (about 1.5 km less melt produced for a decrease of 7 mm/a to 4 mm/a in effective spreading rates, ESR) but not enough to produce near-amagmatic spreading in the most oblique regions of the ridge, unless associated with an anomalously cold and/or depleted mantle source. Our observations lead us to support models in which mantle upwelling beneath slow and ultraslow ridges is somewhat focused and accelerated, thereby reducing the effect of spreading rate and obliquity on upper mantle cooling and melt supply. To explain why very oblique SWIR regions nonetheless have large outcrops of mantle-derived ultramafic rocks and, in many cases, no evidence for axial volcanism [Cannat et al., 2006; Dick et al., 2003], we develop a model which combines melt migration along axis to more volcanically robust areas, melt trapping in the lithospheric mantle, and melt transport in dikes that may only form where enough melt has gathered to build sufficient overpressure. These dikes would open perpendicularly to the direction of the least compressive stress and favor the formation of orthogonal ridge sections. The resulting segmentation pattern, with prominent orthogonal volcanic centers and long intervening avolcanic or nearly avolcanic ridge sections, is not specific to oblique ridge regions. It is also observed along the SWIR and the arctic Gakkel Ridge in orthogonal regions underlain by cold and/or depleted mantle.

Components: 15,980 words, 16 figures, 2 tables.

Keywords: mid-ocean ridges; melt supply; mantle melting; magmatic segmentation.

Index Terms: 3619 Mineralogy and Petrology: Magma genesis and partial melting (1037); 3035 Marine Geology and Geophysics: Midocean ridge processes.

Received 5 May 2007; **Revised** 16 August 2007; **Accepted** 4 December 2007; **Published** 1 April 2008.

Cannat, M., D. Sauter, A. Bezos, C. Meyzen, E. Humler, and M. Le Rigoleur (2008), Spreading rate, spreading obliquity, and melt supply at the ultraslow spreading Southwest Indian Ridge, *Geochem. Geophys. Geosyst.*, 9, Q04002, doi:10.1029/2007GC001676.

1. Introduction

[2] The melt supply per increment of plate separation (henceforth called melt supply) at mid-ocean ridges is predicted to dramatically decrease below a critical spreading rate. This is because upwelling velocities in the subaxial mantle are also expected to decrease, leading to a thickening of the thermal boundary layer and thereby reducing the height of the melting regime [Reid and Jackson, 1981]. However, model predictions for the critical spreading rate below which this effect would become significant are variable [see White *et al.*, 2001, Figure 24], because different models predict different relations between spreading rate and mantle upwelling velocity. This variability results from the sensitivity of melt supply models to poorly constrained parameters of the melting region, such as mantle viscosity, the existence of buoyant instabilities, and the efficiency of melt extraction and focusing beneath the ridge [Bown and White, 1994; Spiegelman and McKenzie, 1987]. Low mantle viscosity, in particular, is expected to favor focusing of the mantle corner flow, and therefore higher upwelling velocities beneath the ridge [Spiegelman and McKenzie, 1987], thus diminishing the effect of upper mantle cooling. Slow, and ultraslow ridges such as the Southwest Indian Ridge (SWIR; full spreading rate: $\sim 14 \text{ mm a}^{-1}$ [DeMets *et al.*, 1994; Patriat and Segoufin, 1988]), which constitute end-members of the global spectrum of ridges, are natural laboratories for testing the potential control exerted by spreading rate on mantle melting.

[3] Seismic data have pointed out the existence of a reduction in oceanic crustal thickness at full spreading rates below 15 mm a^{-1} [Bown and White, 1994; White *et al.*, 2001]. In addition, recent observations suggest that some segments of the SWIR, which are strongly oblique with respect to the direction of plate motion, have a reduced melt

supply [Dick *et al.*, 2003]. Indeed, in these segments, positive gravity anomalies are associated with extensive axial outcrops of serpentinized mantle-derived peridotites [Dick *et al.*, 2003]. This reduction in melt supply has been ascribed to a decrease in the rate of mantle upflow, in proportion to a parameter called Effective Spreading Rate (ESR) and defined as the half-spreading rate resolved in the ridge-perpendicular direction [Dick *et al.*, 2003].

[4] This effect is proposed to be strongest in the highly oblique region of the SWIR located between 10°E and 16°E (ridge region 1 in Figure 1), which has a calculated ESR value of only 3.9 mm a^{-1} [Dick *et al.*, 2003]. Such a low value would correspond to near-zero melt production for mantle melting models with a high-viscosity passively uprising mantle [Phipps Morgan *et al.*, 1987; Reid and Jackson, 1981]. The mean axial depth in this highly oblique region of the SWIR, however, is not significantly greater than in the adjacent region of nearly orthogonal-spreading (region 2 in Figure 1; ESR of 6.7 mm a^{-1}). Mean axial depths calculated over sufficiently long portions of mid-ocean ridges have been proposed to vary as a function of crustal thickness and mantle temperature, two parameters that are linked to the melt supply [Klein and Langmuir, 1987]. Therefore, the observation of similar regional axial depths could indicate that these two regions of contrasted ridge obliquity, have overall comparable melt supplies. This has motivated us to carefully examine the relationship proposed by Dick *et al.* [2003] between ESR and melt supply at ultraslow ridges, by comparing melt supply variations estimated at regional and segment scales along the SWIR.

[5] We first use mean axial depths and sodium contents of basalts as melt supply indicators for 11 ridge regions, each extending for more than 240 km along axis (Figure 1). We then use gravity anoma-

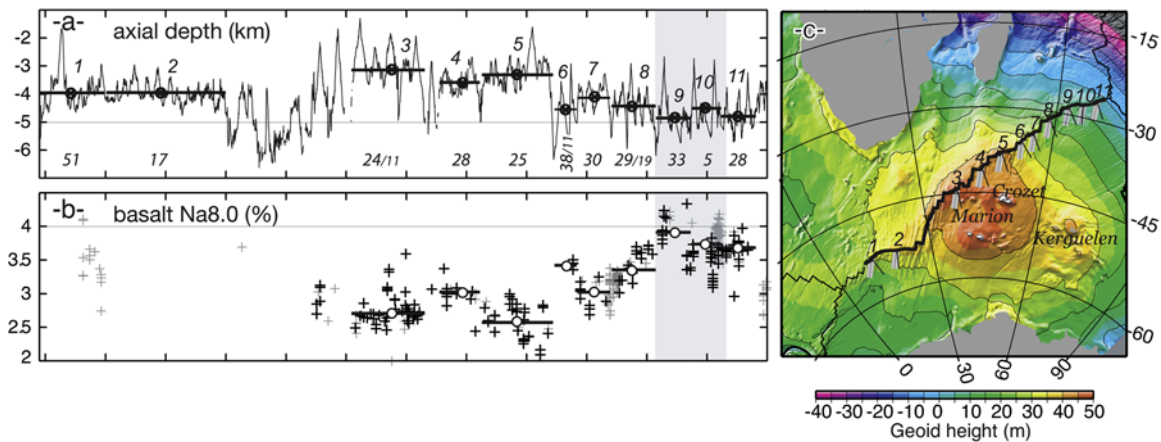


Figure 1. (a) Axial depth, (b) basalt $\text{Na}_{8.0}$ content, and (c) geoid elevation map for the Southwest Indian Ridge. Regional averages of axial depth (Figure 1a) and basalt $\text{Na}_{8.0}$ content (Figure 1b) for the 11 ridge regions (Table 1) are shown as dots and horizontal bars. Regions 9 and 10 are shaded. Data points in Figure 1b are averages per bins of 0.1° in longitude along the ridge axis. Basalt chemistry data are from the Ridge Petrological Data Base (thin grey crosses [Lehnert *et al.*, 2000]; complete references in Table 1) and from the EDUL and SWIFT cruises of R/V *Marion Dufresne* (black crosses [Meyzen *et al.*, 2003] and unpublished data). Figures 1a and 1c also show the ridge's obliquity, defined as the angle between spreading direction (thick grey line in Figure 1c) and a line orthogonal to the ridge axis (thin black line in Figure 1c). Obliquity values calculated for the NUVEL1A plate kinematics model [DeMets *et al.*, 1994] are shown in italics below the bathymetric profile in Figure 1a; smaller values in smaller types for regions 3, 6, and 8 correspond to obliquity that is not accommodated by transform offsets (see text).

lies, geological observations, and seismic data, as indicators for smaller-scale variations of the ridge's melt supply in adjacent ridge regions. We focus on two well-documented adjacent regions of the eastern SWIR, which exhibit contrasting obliquities (regions 9 and 10 in Figure 1). The rationale for this approach at different scales is that while regional (>200 km) melt supply variations should directly reflect flow and melting in the subaxial asthenospheric mantle, melt supply variations at the scale of individual ridge segments (<200 km) may also incorporate the effects of along-axis melt transport and redistribution at the base of, or within the axial lithosphere. For example, melt extracted from the melting region could be guided along axis by a sloping isotherm at the base of the lithosphere [Magde and Sparks, 1997]. Melt may also crystallize in the mantle and never reach the crust [Cannat, 1996], or be redistributed by dikes over along-axis distances of tens of kilometers [Dick, 1989; Smith and Cann, 1999]. Variations of crustal thickness at segment scale may thus reflect vertical and along-axis melt transport, rather than, or in addition to, variations in the melt productivity of the subaxial mantle. Combining observations at regional and segment scales enables us to address this point and to discuss the respective roles of ESR, mantle temperature and compositional heterogeneity, and

along-axis melt transport in controlling the ridge's melt supply.

2. Spreading Obliquity and Large-Scale Melt Supply Variations Along the SWIR

[6] We consider the SWIR between 10°E and 69°E of longitude, where we have defined 11 ridge regions, separated either by sharp changes in ridge orientation, or by major transform faults (Figure 1 and Table 1). Regional values of the SWIR obliquity relative to the spreading direction, calculated for each region with the NUVEL1 plate kinematics model [DeMets *et al.*, 1994], vary from 51° in region 1 to 5° in region 10 (Figure 1a). Reconstructions proposed by Patriat and Segoufin [1988] for the period since magnetic anomaly 5 (~ 10 Ma ago) yield similar obliquity values. Regions 3, 6 and 8 contain moderate offset (less than 50 km) transform faults that accommodate a part of this obliquity. In other regions, the ridge axis itself is oblique, as discussed by Dick *et al.* [2003]. Effective spreading rates (ESR) calculated for NUVEL1 spreading vectors, vary from 4.25 mm a^{-1} in region 1 (equivalent to the 3.9 mm a^{-1} value of Dick *et al.* [2003] for this same region) to 7.05 mm a^{-1} in regions 3 and 6 (Figure 2). The three-plate kinematic model of Horner-Johnson *et al.* [2005] yields similar ESRs in regions 3 to 11, but higher

Table 1. Summary of the Characteristics of the 11 Southwest Indian Ridge Regions Identified in Figure 1^a

Region	From Lon °E	To Lon °E	Ridge Length, km	Mean Ridge Azimuth, deg	Regional Axial Depth, m	Std, m	Regional MBA, mGal	Std, mGal	Regional Basalt Na8.0, wt%	Std, wt%	Number of Glass Samples Analyzed	References ^b
1	9.69	14.11	368	73.8	3971	674	-59	17	3.49	0.26	9	1
2	14.18	25.14	758	101.8	3961	351	-54	20	-	-	-	
3	35.55	41.53	680	78.2	3134	680	-114	24	2.71	0.28	53	1, 2, 3
4	42.81	46.05	362	70.1	3598	342	-86	27	3.02	0.18	14	1, 3, 4
5	46.23	52.31	654	69.7	3304	628	-90	30	2.61	0.25	38	2, 3, 5, 6
6	52.37	54.13	240	56.3	4508	742	-14	44	3.44	0.06	4	6
7	54.18	57.02	330	64.3	4091	430	-37	20	3.03	0.17	39	5, 6, 7, 8
8	57.11	60.75	453	61.3	4435	516	-26	24	3.35	0.2	57	5, 6, 7, 8, 9
9	60.85	63.67	395	58.1	4742	586	1	24	3.89	0.32	19	5, 6, 10
10	63.67	66.13	260	82.4	4542	619	-15	32	3.72	0.25	120	5, 6, 9, 11, 12
11	66.36	69	352	58.8	4806	471	-32	12	3.67	0.08	49	5, 6, 9, 11, 12

^aThese regions are separated by sharp changes in ridge orientation or by transform faults. Region 1, longitude 9.69°E to a sharp change in ridge orientation at 14.11°E; region 2, 14.11°E to Du Toit Fracture Zone; region 3, Prince Edward FZ to Discovery II FZ; region 4, Discovery I FZ to Indomed FZ; region 5, Indomed FZ to Gallieni FZ; region 6, Gallieni Fz to Gauss FZ; region 7, Gauss FZ to Atlantis II FZ; region 8, Atlantis II FZ to Melville FZ; region 9, Melville FZ to a change in ridge trend at longitude 63.67°E; region 10, 63.67°E to a change in ridge trend at 66.13°E; region 11, 66.13°E to 69°E. Regional axial depths are calculated from shipboard multibeam data (Dick et al. [2003], Grindlay et al. [1998], Sauter et al. [2001], Mendel et al. [1997], and data from the SWIFT cruise of R/V *Marion Dufresne*). Mantle Bouguer gravity anomalies were calculated by Georgen et al. [2001] from satellite gravity data and GEBCO bathymetry. Na_{8.0} (sodium content corrected for fractional crystallization to a common MgO content of 8%) was calculated using sodium and magnesium contents of basalt glass samples, with the empirical formula of Klein and Langmuir [1987]. Samples with MgO < 6.5% or MgO > 8.5% were excluded from this calculation. Basaltic glass samples collected during the SWIFT and EDUL cruises of R/V *Marion Dufresne* were analyzed on the CAMPARIS electron microprobe in Paris. Other glass data were downloaded from the Petrological Database [Lehnert et al., 2000]. We did not correct the data for potential interlaboratory bias.

^bReferences for basalt glass compositions are as follows: 1, *le Roex et al.* [1992]; 2, *Mahoney et al.* [1992]; 3, SWIFT; 4, *Schiano et al.* [1997]; 5, *Meyzen et al.* [2003]; 6, EDUL; 7, *Dick et al.* [1991]; 8, *Johnson and Dick* [1992]; 9, *Robinson et al.* [1996]; 10, *Natland* [1991]; 11, *Price et al.* [1986]; 12, *Robinson et al.* [2001].

spreading rates and ESRs in regions 1 and 2 (Figure 2).

[7] Regional averages of axial depth, and of the sodium contents of basalts, are commonly used to evaluate melt supply variations along the mid-ocean ridge system [Klein and Langmuir, 1987]. In these studies, axial depths are averaged over long portions of the ridge and interpreted as isostatic. They are therefore expected to become shallower with increasing crustal thickness and

mantle temperature, two parameters that are related to the ridge's melt supply [Klein and Langmuir, 1987]. The sodium content of primary melts generally decreases as melting of the mantle source proceeds to higher rates. Once sodium contents of basaltic glasses have been corrected for the effect of low-pressure fractional crystallization to a common MgO content of 8 wt.%, they can be used for estimating the mean extent of melting in the volume of mantle processed through the melting

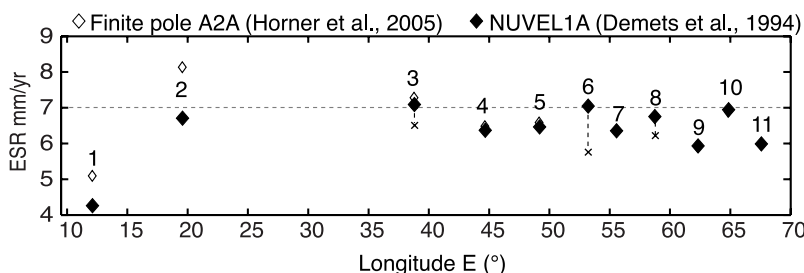


Figure 2. Effective spreading rate (ESR; half-spreading rate resolved in the ridge-perpendicular direction [Dick et al., 2003]) for the 11 ridge regions defined in Figure 1, calculated using the NUVEL1 plate motion model [DeMets et al., 1994] or the three-plate (Somalia, Nubia, and Antarctica) model of Horner-Johnson et al. [2005]. Two ESR values are shown for regions 3, 6, and 8: corrected (diamonds) and noncorrected (crosses) from internal transform offsets.

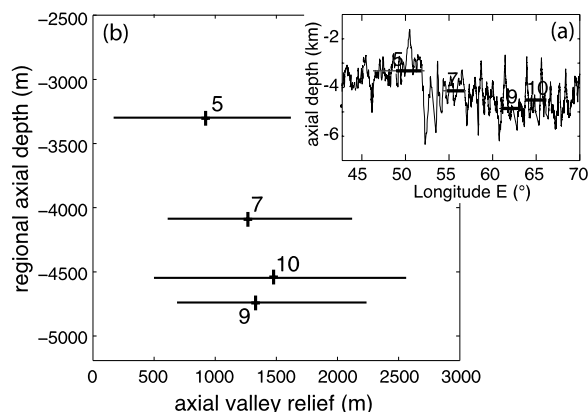


Figure 3. Range of axial valley relief in four portions of the SWIR that have adequate bathymetric coverage [Cannat et al., 2006; Mendel et al., 2003]. These four ridge portions are shown by thick horizontal bars in Figure 3a. They belong to regions 5, 7, 9, and 10 (Table 1 and Figure 1), shown by thin horizontal bars in Figure 3a. Axial valley relief is measured for across-axis profiles spaced by 10 km. It is defined as the contrast in depth between the top of the highest axial valley wall and the bottom of the axial valley [Small, 1998]. Horizontal bars in Figure 3b show the range of axial valley relief values, and crosses show the average values in each region. We infer that dynamic deepening of the axial valley floor could represent half of these average values (500 to 700 m), the other half being accommodated by dynamic uplift of the axial valley walls [Weissel and Karner, 1989].

region per increment of spreading [Klein and Langmuir, 1987]. To perform this estimate and that of melt supply, however, it is necessary to infer the sodium content of the mantle source entering the melting regime, and to adopt simple mantle flow and melt extraction configurations [Langmuir et al., 1992]. Rare Earth Elements composition of basalts can also serve as proxy for mean melting extent, using similar assumptions [White et al., 1992]. Global variations of regional axial depth, sodium and REE contents of basalts along the Earth's ridge system are correlated, and estimated melt supply generally fits seismic crustal thickness, where available [Klein and Langmuir, 1987; White et al., 1992].

[8] Regional averages for axial depth along the SWIR vary between 3134 m in region 3, and 4742 m in region 9 (Figure 1 and Table 1) and are well correlated with axial values of the mantle Bouguer gravity anomaly (MBA), averaged over the same regions (Table 1). This correlation (with a linear correlation coefficient R^2 equal to 0.9) indi-

cates that regional axial depths do vary with the density structure of the ridge axis and therefore supports the use of these regional depths as indicators of axial crustal thickness and/or mantle temperature. Axial depth at slow spreading ridges may not, however, be considered as strictly isostatic because it also includes a dynamic component related to the formation of the axial valley [Neumann and Forsyth, 1993; Small, 1998]. In order to evaluate the contribution of this nonisostatic component, to variations of regional axial depths measured along the SWIR, we have compared axial valley relief in four regions of contrasted regional axial depth, for which we had adequate bathymetric coverage (Figure 3). We find that the mean axial valley relief is equal to 921 ± 391 m in the shallowest part of ridge region 5, to 1266 ± 432 m in the eastern half of region 7, and to 1329 ± 460 m and 1479 ± 518 m, respectively, in regions 9 and 10. Assuming that half of this relief corresponds to dynamic deepening of the axis (while the other half corresponds to dynamic uplift of the axial valley walls [Weissel and Karner, 1989]), we can thus estimate that the nonisostatic contribution to the 1.4 km regional axial depth contrast between regions 5 and 9 is only of the order of 200 m. Another potential limitation of the use of regional axial depth as a proxy for melt supply is the possibility that the crust also includes variably serpentinized mantle-derived peridotites. This would result in shallower isostatic axial depths for a given mantle temperature and melt thickness. We will come back to this possibility in the discussion.

[9] On-axis basalts collected along the SWIR contain on average 7.72 wt.% of MgO, for an average silica content of 50.42 wt.%. Their average K_2O/TiO_2 ratio of 0.21 ± 0.17 is higher than those of basalts from the Mid Atlantic and East Pacific ridges, which are respectively of 0.18 and 0.12 [Su, 2002]. This suggests that SWIR primary magmas are, on average, more enriched than those of the Mid Atlantic and East Pacific ridges. To gain further insight into the processes occurring during mantle melting and melt extraction, it is necessary to first correct major-element compositions for the effect of low-pressure fractionation. We thus normalized the sodium content of SWIR basalts to 8 wt.% MgO, following the procedure described by Klein and Langmuir [1987]. Basaltic glasses from regions #3 and #4 (A. Bezos et al., manuscript in preparation, 2008), and from region #1 [le Roex et al., 1992; Standish et al., 2006] have anomalously high K_2O/TiO_2 ratios. It is worth noting that the most enriched samples in regions #3 and #4 are

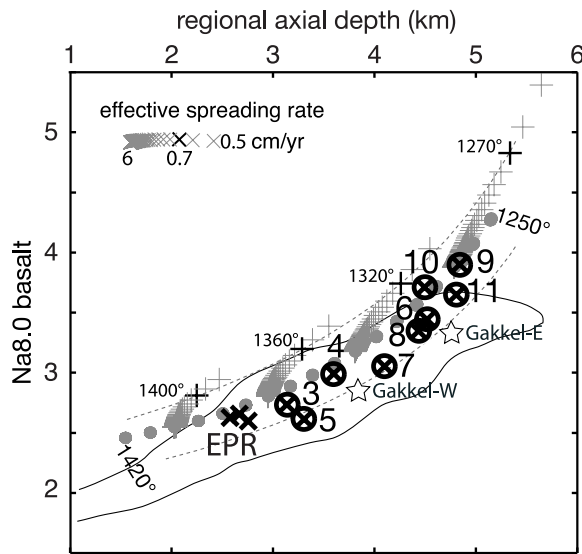


Figure 4. Regional averages of axial depth and basalt $\text{Na}_{8.0}$ content for SWIR regions 3 to 11 (crossed circles; standard deviations listed in Table 1) compared to model values. Model values are shown as grey dots, and crosses have been calculated for initial mantle temperatures ranging from 1250°C to 1420°C at 100 km depth (equivalent to mantle potential temperatures [McKenzie, 1984] of 1220°C to 1390°C), effective spreading rates (ESR) ranging between 60 mm a^{-1} (grey dots spaced by 10°C) and 5 mm a^{-1} (crosses at 1 mm a^{-1} interval, thicker crosses for ESR equal to 7 mm a^{-1}), and an initial mantle Na_2O weight content of 0.27%. Grey dots correspond to adiabatic mantle melting. The two dashed curves are calculated for an ESR of 7 mm a^{-1} and two initial mantle Na_2O weight contents: 0.22% for the bottom curve and 0.27% for the top curve. SWIR data points are best fitted by 7 mm a^{-1} model curves calculated for mantle sodium contents between 0.22 and 0.25%. Regional axial depths and basalt $\text{Na}_{8.0}$ values in 3 regions of the fast spreading East Pacific Rise (EPR) (thick crosses [Cannat et al., 2004]) and in the eastern and western parts of the ultraslow Gakkel ridge in the Arctic [Michael et al., 2003] are shown for comparison. Note that EPR values plot near the modeled curve for adiabatic melting for a mantle temperature near 1370°C and 0.27 wt% initial sodium. The outlined field is the global MORB array of Langmuir et al. [1992].

basaltic andesites with low MgO and high SiO_2 contents (Bezou et al., manuscript in preparation, 2008). In addition, basaltic glasses from the easternmost SWIR (regions 9 to 11) display unusual major and trace element compositions relative to the global mid-ocean ridge basalt (MORB) systematics. In particular, Meyzen et al. [2003] have reported depleted heavy Rare Earth elements and

anomalously low $\text{Ti}_{8.0}$ contents with respect to the global $\text{Na}_{8.0}$ - $\text{Ti}_{8.0}$ MORB array.

[10] Despite these compositional complexities, regional averages of $\text{Na}_{8.0}$ content of SWIR basalts are well correlated with regional axial depths (Figures 1 and 4; linear correlation coefficient R^2 equal to 0.84) and overlap, except for regions 9 and 10, with the global $\text{Na}_{8.0}$ -depth MORB array of Klein and Langmuir [1987] and Langmuir et al. [1992]. By contrast, there is no correlation between ridge obliquity and regional axial depth and basalt $\text{Na}_{8.0}$ content: region 10 falls near the highest basalt sodium content end of the spectra, while it has the smallest ridge obliquity and an ESR similar to those of regions 3 and 6 (Figure 2). Region 1 has the largest obliquity and smallest ESR (Figure 2), but an intermediate regional axial depth (Figure 1a). Region #3, close to Marion and Crozet islands, has the shallowest axial depth, and the lowest basalt $\text{Na}_{8.0}$ content. Both indicators steadily increase eastward, suggesting a progressive eastward decrease of the ridge's melt supply. The increase in $\text{Na}_{8.0}$ contents of basalts sampled over regions 5 to 9 is correlated with a decrease in their $\text{Fe}_{8.0}$ contents [Meyzen et al., 2003]. This is consistent with an eastward decrease in the mean pressure of mantle melting [Klein and Langmuir, 1987], and suggests lower mantle temperature in the east [Meyzen et al., 2003].

[11] In order to further evaluate these results, we use a one-dimensional (1-D) analytical model of mantle melting derived from Langmuir et al. [1992], which takes into account the effect of upper mantle conductive cooling at the top of the melting regime. Model parameters are listed in Table 2; further details are given by Cannat et al. [2004]. This model allows us to predict melt supply, isostatic axial depths and basalt $\text{Na}_{8.0}$ contents, for a given ESR and mantle temperature. Owing to the large uncertainties attached to such simplified mantle melting models, we will not use these predictions literally, but instead as a guide for discussion and comparisons. The model assumes that mantle upflow beneath the ridge occurs at velocities equal to the ESR, which would be close to the predictions of corner flow 2-D models with a high-viscosity mantle [Phipps Morgan et al., 1987; Reid and Jackson, 1981]. Being one dimensional, our model does not, however, take lateral heat loss into account and therefore predicts hotter axial temperatures and higher melt production for a given ESR, than these high-viscosity corner flow models. Instead, the sensitivity of our 1-D model to

Table 2. Parameters Used in 1-D Mantle Melting Model^a

Name and Unit of Parameter	Abbreviation and Value Used in Melting Model
Mantle upwelling velocity, cm a ⁻¹	u = 0.1 to 6
Mantle adiabatic temperature gradient, deg km ⁻¹	adgrad = 0.3
Latent heat of melting in mantle, cal g ⁻¹	Hf = 150
Mantle heat capacity, cal g ⁻¹	cp = 0.3
dT/dF, deg % ⁻¹	dTdF = 3.5
dT/dF for mantle that has already melted by 22%	dTdF22 = 6.8
Thermal diffusivity of mantle rocks, m ² s ⁻¹	k = 8.04.10 ⁻⁷
Upper boundary for conductive cooling model, km	za = 0
Depth, km, at which conductive cooling is assumed to be negligible	zzero = 100
Maximum depth of model, km	zz = 200
Temperature at za, °C	Tza = 1
Maximum depth of hydrothermal cooling, km	zhydr = 5
Enhanced conductivity in domain of hydrothermal circulation	coeff = 8
Compensation depth, km, for regional isostatic compensation	zcomp = zz
Axial depth, km, for reference column	zref = 3
Melt thickness, km, for reference column	mref = 6.06
Mean mantle density, kg m ⁻³ , for reference column	dmref = 3313.9
Mantle thermal expansion coeff., deg ⁻¹	exptherm = 3.10 ⁻⁵
Mantle compressibility modulus, kbar ⁻¹	modcomp = 10 ⁻³
Density, kg m ⁻³ , of fertile mantle in spinel-garnet facies (25°C, 1 atm)	dmsg = 3340
Density, kg m ⁻³ , of residual mantle (F:30%) in spinel-garnet facies (25°C, 1 atm)	dmd = 3295
Density of crust, kg m ⁻³	dc = 2700
Density of water, kg m ⁻³	de = 1010

^aMelt sodium contents are calculated for pooled fractional melts as by *Langmuir et al.* [1992]. A complete description of this model is given by *Cannat et al.* [2004].

mantle cooling at slow and ultraslow spreading rates (Figure 5) is similar to that of the corner flow 2-D model of Bown and White [Bown and White, 1994], which includes the control of the lithosphere wedge angle at slow spreading rates on mantle upwelling velocities [Spiegelman and McKenzie, 1987]. This control causes mantle upwelling velocities to become higher than the ESR at the slowest ridges, thus diminishing the effect of upper mantle cooling.

[12] SWIR values for regional axial depth and basalt Na_{8,0} content are consistent with modeled values (Figure 4), although they display lower sodium contents for a given axial depth than the trend calculated with an initial sodium content of 0.27 wt% for the source, and an ESR of 7 mm a⁻¹. The same shift is observed for the Arctic Gakkell ridge (Figure 4). Such a shift would be expected for a lower initial mantle sodium content, or for less pronounced mantle cooling from above than predicted in the model. This shift, or part of this shift, could also be due to the formation of a deep axial valley [Small, 1998]. Mean axial valley relief shown in Figure 3 suggests for example that regional axial depths at the SWIR could be shifted by 400 to 700 m down from isostatic values.

[13] The trend defined by SWIR lavas and regional depths in Figure 4 can be reproduced quite closely by along-axis variations in melt supply, producing a magmatic crust whose thickness ranges from about 6 km in region 3 to only 2 to 3 km in the easternmost regions 9 to 11 (Figure 6). These latter values are of the same order or smaller than the average seismic crustal thickness of ~3.5 km determined near 66°E in region 11 [Minshull et al., 2006; Muller et al., 1999]. This large-scale variation of the ridge's melt supply could be explained by a change of about 60°C in the temperature of the subaxial mantle from the longitude of Marion Island (regions 3 and 4), to the easternmost SWIR (Figure 4) [Cannat et al., 1999], consistent with the broad geoid high observed over the same area (Figure 1c). Basalts from the easternmost SWIR also have very specific compositions [Meyzen et al., 2003], while most basalts from regions #1 [le Roex et al., 1992; Standish et al., 2002], and regions #3 and #4 (Bezous et al., manuscript in preparation, 2008) are enriched. Mantle compositional heterogeneities may thus also contribute to the large-scale changes in melt productivity observed along the SWIR. Correcting regional axial depths for the possible dynamic contribution of the axial valley, would lead to model melt thickness about 1 km larger in each

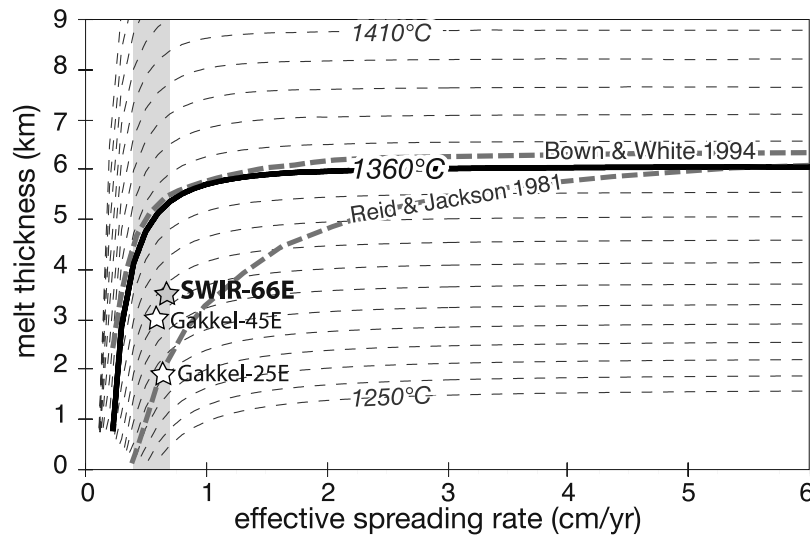


Figure 5. Predicted melt supply (thickness of melt produced per increment of plate separation) as a function of ESR (equal to half-spreading rate for orthogonal spreading ridges). Mantle temperatures range between 1250 and 1450°C at 100 km depth (dashed curves). Solid line corresponds to a mantle of “normal temperature” (defined as corresponding to the production of a 6 km-thick magmatic crust in adiabatic conditions; in our model, it is equal to 1360°C). Modeled curves for the corner flow models of *Bown and White* [1994] and *Reid and Jackson* [1981] are shown for comparison (thick dashed grey lines). Shaded domain shows range of ESR along the SWIR (Figure 2). The grey star corresponds to the average of seismic crustal thickness at 66°E along the SWIR (in region 11 [Muller et al., 1999]). Open stars are crustal thickness averages between 25°E and 30°E and 40 and 50°E along the eastern part of the arctic Gakkel Ridge [Jokat et al., 2003].

ridge region, but would not have a significant effect on the amplitude of this large-scale variation (Figure 6).

3. Melt Supply Variations in Adjacent SWIR Regions of Contrasted Obliquity

[14] The effect of ridge obliquity on melt supply is not clear at the scale of Figure 1, because it operates on a mantle source that appears significantly heterogeneous, and is in particular affected by a broad and large amplitude anomaly associated with the Marion-Crozet geoid high (Figure 1c). In this section, we examine two pairs of adjacent regions with contrasted obliquity: regions 1 and 2, and regions 9 and 10 (Figure 1). Very large variations in mantle temperature are unlikely between these adjacent ridge regions, so that we may hope to evaluate the effect of ridge obliquity on melt production.

3.1. Ridge Regions 1 and 2

[15] Region 1 is 368 km-long, with two robust volcanic centers, and 2 intervening deeper axial sections, with widespread outcrops of serpentinitized peridotite [Dick et al., 2003]. One of these

deeper sections is 184 km-long, with an obliquity of 56° [Dick et al., 2003]. The two volcanic centers (Joseph Mayes seamount and Narrowgate segment) correspond with thicker crust, with volcanic ridges and faults that trend orthogonal to spreading over distances of about 40 km [Dick et al., 2003]. Region 2 comprises two subregions [Grindlay et al., 1998]: to the west of longitude 20°E, the ridge is shallower, with more negative MBA anomalies; to the east, it is about 200 m deeper on average, and MBA anomalies increase steadily eastward. Regional axial depths and MBA values for regions 1 and 2 (Table 1) suggest an intermediate melt supply, with an estimated melt thickness of 4 km (Figure 6). The model shown in Figure 6 predicts near-normal mantle temperature in region 1 (ESR value close to 4 mm a⁻¹), with a substantial decrease of melt supply due to high ridge obliquity: by about 1.2 km compared to melt supply predicted at the same mantle temperature for an ESR of 7 mm a⁻¹, and by about 2 km compared with a purely adiabatic mantle cooling setting (corresponding to ESR values ≥ 3 cm a⁻¹ in the conditions of our model; Figure 5). Region 2 (ESR value close to 7 mm a⁻¹) may then be inferred to have a lower temperature (by about 20°), or less fertile mantle. This would be consis-

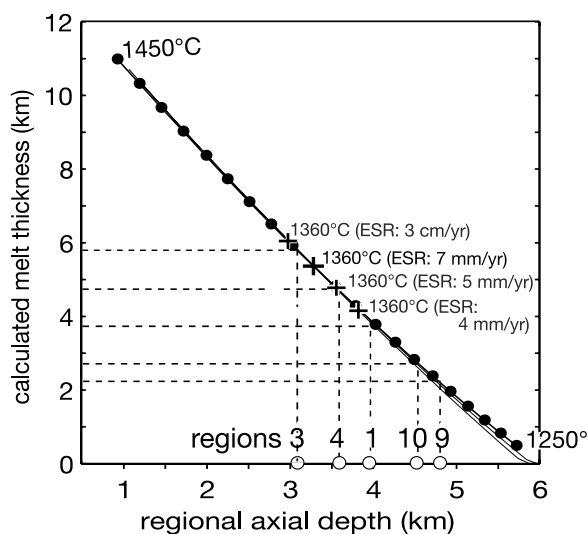


Figure 6. Thickness of melt produced per increment of plate separation and regional axial depth calculated using the same model as in Figures 4 and 5 for initial mantle temperatures ranging between 1250°C and 1450°C at 100 km depth and for ESR values of 7 mm a⁻¹ (solid line with dots calculated every 10°C), 5 mm a⁻¹, and 4 mm a⁻¹ (thinner lines). Decreasing the ESR does not significantly change the shape of these calculated melt thickness versus regional axial depth curves. It does, however, shift these curves to the bottom right of the diagram, so that a given melt thickness is obtained for progressively higher mantle temperatures. Crosses indicate calculated melt supply and isostatic axial depth calculated for a 1360°C mantle, and ESR values of 3 cm a⁻¹ (adiabatic mantle cooling) and 7, 5, and 4 mm a⁻¹. Increasing the sensitivity of mantle melting to ESR variations (for example, from the *Bown and White* [1994] to the *Reid and Jackson* [1981] model shown in Figure 5) would result in a wider spread for these calculated values. Regional axial depths are represented for SWIR regions 1, 3, 4, 9, and 10 (crossed circles, as in Figure 1). They correspond to modeled melt thicknesses ranging between 2 and 6 km. Correcting average axial depths for the possible dynamic contribution of the axial valley (estimated as 500 to 700 m; Figure 3) shifts predicted mantle temperatures up by about 20°C and predicted melt thicknesses by about 1 km.

tent with the westward decrease of the geochemical influence of the Bouvet Plume on basalts collected between 9 and 25°E [*Standish et al.*, 2006], and with the eastward deepening of the ridge and increase of axial MBA values measured within region 2 [*Grindlay et al.*, 1998].

[16] Using regional axial depth as a proxy for melt supply, we therefore reach the intermediate conclusion that the effect of the small ESR in region 1 is a reduction of melt thickness by about 2 km,

significantly less than the near-complete melt supply shutdown proposed by [*Dick et al.*, 2003]. Our approach assumes that the mantle flow regime does not change in fundamental ways in these two regions. It has, however, been proposed that the pronounced contrast in ridge morphology within region 1, between narrow volcanic centers, and long oblique sections of the axis, could be explained in the frame of a 3-D mantle flow regime, with corner flow beneath the oblique sections, and buoyant upwelling beneath the volcanic centers [*Dick et al.*, 2003; *Standish et al.*, 2006]. To account for this possibility, we now focus our regional approach on two subsets of regions 1 and 2: the 184 km-long, deep oblique segment at longitude 11.8°E to 14.2°E [*Dick et al.*, 2003], and the 280 km-long, western and shallowest part of region 2, between longitude 16°E and 20°E [*Grindlay et al.*, 1998]. We find an average axial depth of 4113 ± 316 m in the oblique segment (local ESR equal to 3.85 mm a⁻¹), and of 3803 ± 338 m in the western part of region 2 (local ESR equal to 6.8 mm a⁻¹). In order to get an estimate of the topographic effect of high ridge obliquity in the long oblique segment of region 1, we should add to this 300 m difference in axial depth, the effect of possible differences in mantle temperature or composition between the two regions. Assuming that this effect is equivalent to the topographic effect of a 20°C difference in mantle temperature, or about 500 m (Figure 6), we thus estimate that the topographic effect of the lower ESR in the long oblique segment of region 1 is about 800 m, yielding a calculated melt supply deficit of about 1.6 km compared to the melt thickness expected at an ESR of 7 mm a⁻¹ (Figure 6). This is to first order consistent with the prediction of our melting model: plotted for an ESR of 4 mm a⁻¹ in Figure 6, the average axial depth in the long oblique segment corresponds to a melt thickness of 3.5 km and a mantle temperature of 1350°C, while a mantle of similar temperature is predicted to supply 4.7 km of melt at an ESR of 7 mm a⁻¹, and 5.5 km of melt in adiabatic melting conditions. These predictions may be collectively shifted to higher values if the possible dynamic contribution of the axial valley is taken into account. The melt supply deficit predicted in the long oblique segment is significant, but much less than proposed by *Dick et al.* [2003]. The production of 3.5 km of melt is also in apparent contradiction with dredging observations indicating that the crust in the long oblique segment of region 1 is largely made of mantle-derived

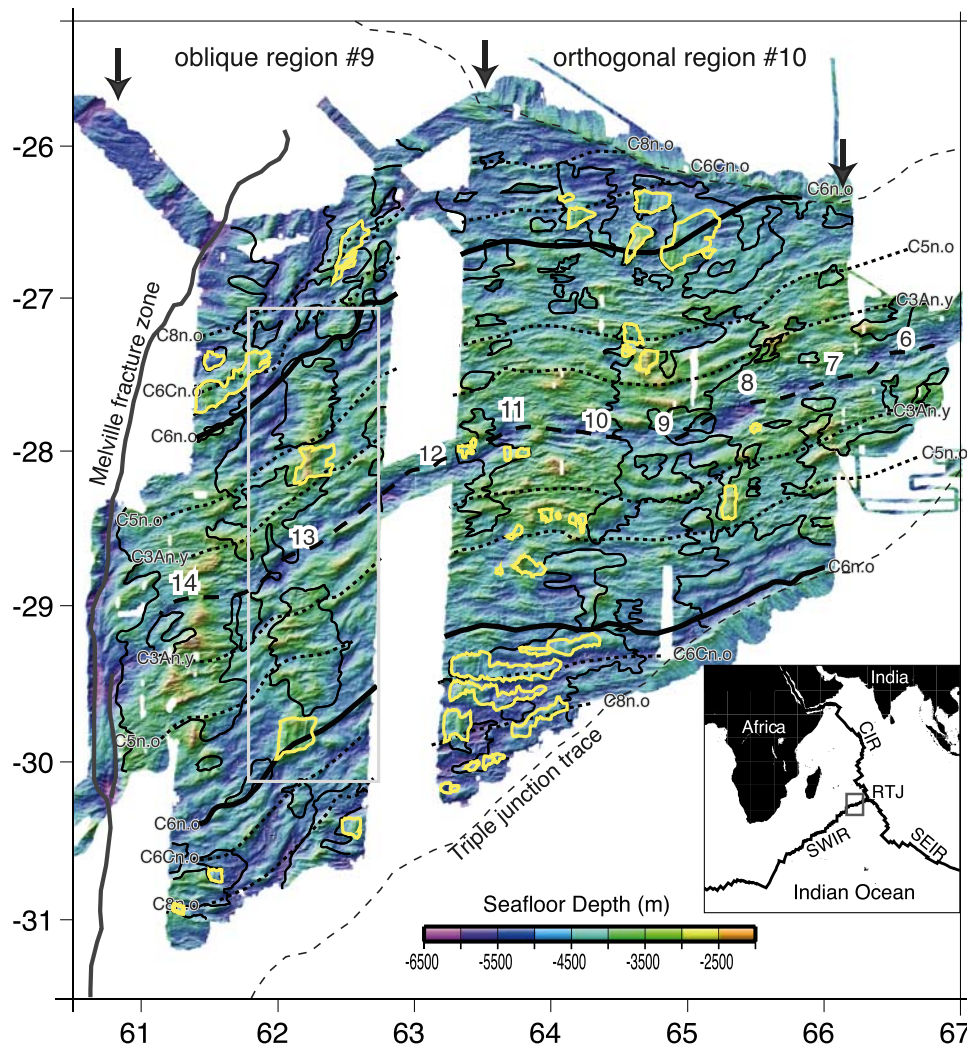


Figure 7. Shaded bathymetry for SWIR regions 9 and 10 [Cannat *et al.*, 2006]. Thin black contours outline terranes with numerous scarps and volcanic cones. Adjacent seafloor has a smooth topography, with no volcanic features [Cannat *et al.*, 2006]. Corrugated seafloor domains, which are inferred to correspond to exhumed detachment fault surfaces, are outlined in yellow. Thick dashed line indicates the Central Magnetic Anomaly. Thinner dashed lines are other magnetic isochrons from Cannat *et al.* [2006]. Isochrons for magnetic anomaly 6 (20.13 Ma [Cande and Kent, 1995]) are shown in black. Ridge segments are defined on the basis of bathymetry and are numbered from 6 to 14 [Cannat *et al.*, 1999]. Inset shows locations of Figures 11 and 16b.

peridotite [Dick *et al.*, 2003]. We will address this paradox in the discussion.

3.2. Ridge Regions 9 and 10

[17] We now examine variations of the melt supply in adjacent regions 9 and 10, as inferred from mean $\text{Na}_{8,0}$, axial depth and MBA variations. These two regions are located in the easternmost part of the SWIR, and they both have overall a very low melt supply, as suggested by large axial depths and high basalt sodium contents (Figure 1). Region 9 has an obliquity of 33° (calculated ESR: 5.9 mm a^{-1}),

while region 10 has near-orthogonal spreading (ESR: 6.9 mm a^{-1}). The contrast in ESR is significantly less than between regions 1 and 2: in our melting model, it corresponds to a difference of only about 0.5 km in melt thickness, for a uniform mantle temperature. Regions 9 and 10, however, have a strong asset for a comparative study: they have both been mapped up to seafloor older than magnetic anomaly 8 (26.5 Ma [Cande and Kent, 1995]), and magnetic anomalies indicate that both the spreading rate and the plate boundary geometry have been stable since at least the time of magnetic anomaly 6 [Cannat *et al.*, 2006]. The

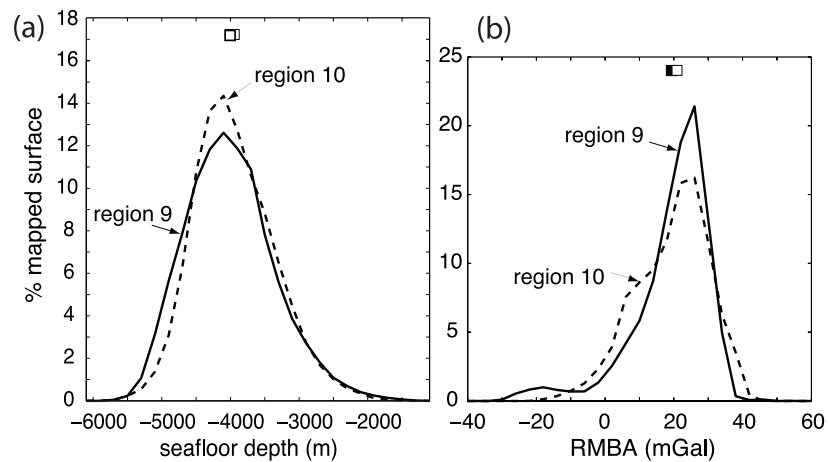


Figure 8. Histograms of (a) seafloor depth and (b) residual mantle Bouguer anomaly (RMBA) for crustal ages younger than 20.13 Ma (magnetic anomaly 6; Figure 7) in regions 9 (for longitude > 61°E) and 10. Percents of mapped surface are counted by bins of 200 m in Figure 8a and of 4 mGal in Figure 8b. In the model used for gravity data processing, the reference crustal thickness is 3.4 km, yielding a RMBA value of 20 mGal [Cannat *et al.*, 2006]. RMBA values < 20 mGal therefore correspond to modeled crust thicker than 3.4 km. Mean values (squares) of seafloor depth and RMBA for the two regions overlap within errors.

effect of spreading obliquity on melt supply can therefore be examined over the past 20 Ma of ridge activity.

[18] The gravity map of regions 9 and 10 shows a striking pattern of irregularly spaced gravity low bull's-eyes [Cannat *et al.*, 2003, 2006]. On axis, these bull's-eyes correspond to three large active volcanic centers (center of ridge segments 8, 11, and 14 in Figure 7) that may be compared to the volcanic centers in region 1 [Dick *et al.*, 2003], and in the deepest section of the arctic Gakkel Ridge [Michael *et al.*, 2003]. Off-axis gravity low bull's-eyes are inferred to correspond to former volcanic centers [Cannat *et al.*, 2003]. The ridge segmentation pattern defined on the basis of bathymetry in this part of the SWIR [Cannat *et al.*, 1999] differs from the more usual, Mid-Atlantic Ridge-type segmentation. At the Mid-Atlantic Ridge, shallower seafloor at segment centers and deeper seafloor at segment ends correspond with, respectively, more negative, and more positive MBA anomalies, which suggest respectively higher and smaller melt supply from the subaxial mantle [Lin *et al.*, 1990]. By contrast, SWIR segments 9 and 12 (Figure 7), for example, have flat along-axis MBA profiles, while segment 10 corresponds to the eastern limb of the broad gravity low associated with segment 11 [Cannat *et al.*, 1999]. This suggests that melt focusing in the subaxial mantle of SWIR regions 9 and 10 operates over scales that are larger than the length of most bathymetrically defined segments [Cannat *et al.*, 2003].

[19] The difference in average axial depths between regions 9 and 10 is small (200 m; Table 1 and Figure 1), but consistent with the prediction of our model for a cold mantle and for the ESR values in each region (Figure 6). It suggests a difference of about 0.5 km in melt supply, which is also consistent with the difference in average MBA at the ridge axis (Table 1). Melt supply variations between the two regions, if due to a smaller ESR in region 9, should however have persisted over the past 20 Ma. Yet, we observe no systematic differences in seafloor depth and residual mantle Bouguer anomaly (RMBA) in the off-axis domains of regions 9 and 10 (Figure 8). This could indicate that there are in fact no differences in the time-integrated melt supply of the two regions. There are, however, marked contrasts between the two regions in the off-axis distribution of seafloor morphologies [Cannat *et al.*, 2006]. We now detail these differences and how they might reveal variations in along-axis melt distribution within each ridge region.

[20] One difficulty here lies in the lack of unambiguous indicators for the ridge's melt supply at scales less than 100 km. Axial depths, when averaged over such short distances, cannot be assumed to reflect isostatic balance. In addition, small-scale variations of the $\text{Na}_{8,0}$ contents of basalts may reflect local heterogeneities of the melting regime, or along-axis melt transport. Seismic crustal thickness is the most relevant melt supply indicator at this scale [White *et al.*, 1992].

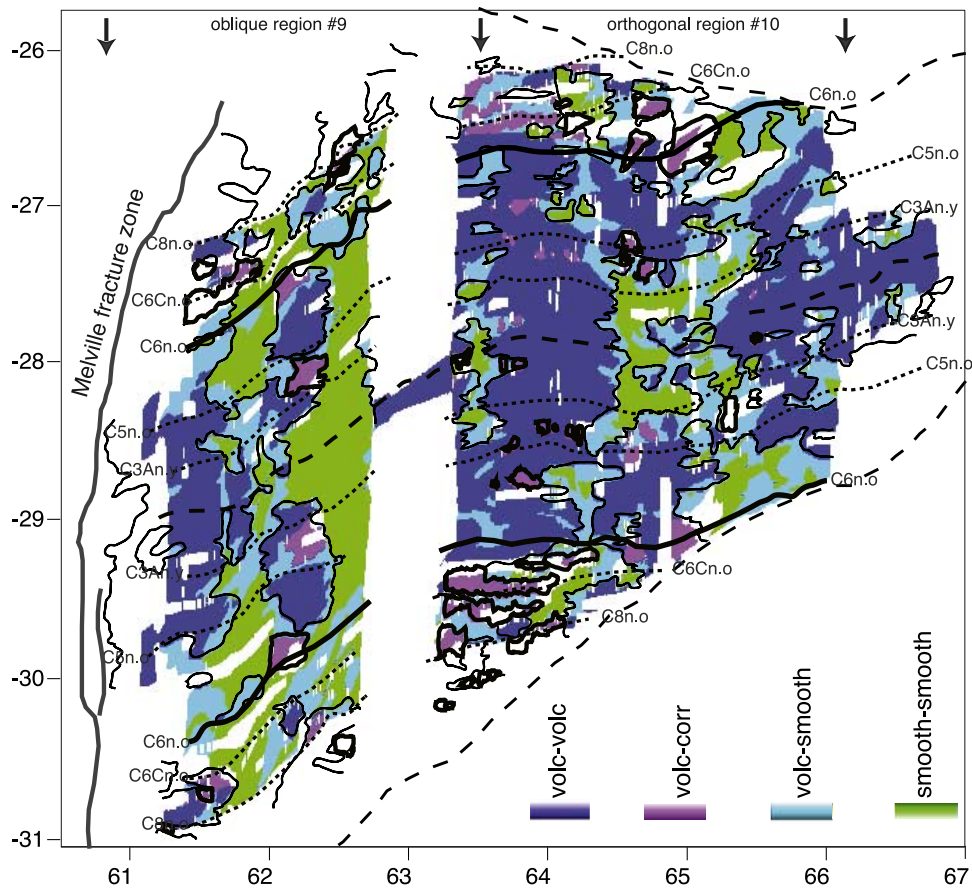


Figure 9. Conjugate pairs of seafloor morphologies which are inferred to have formed simultaneously on each side of the axial valley from the time of magnetic anomaly 8 (26.5 Ma [Cande and Kent, 1995]) to present. Thin black contours indicate volcanic terranes as in Figure 7. Thick black contours indicate corrugated seafloor as in Figure 7. Conjugate seafloor morphologies are reconstructed using plate rotation parameters derived from *Patriat and Segoufin* [1988] and adjusted to fit pickings of magnetic anomalies in regions 9 and 10 (magnetic isochrons shown as in Figure 7). This reconstruction assumes symmetrical spreading, and the plate boundary is interpolated linearly for each age step from our nearest magnetic anomalies pickings. These assumptions add to the uncertainties attached to the plate rotation parameters [Patriat and Segoufin, 1988], and to the delimitation of volcanic, corrugated, and smooth seafloor terrains. This leads to cumulated errors in the order of a few square kilometers.

It should, however, be interpreted with caution because the common observation of outcrops of mantle-derived serpentinized peridotites demonstrates that slow and ultraslow-spread crust does include a nonmagmatic component. Furthermore, some melt may also have crystallized in cooled mantle beneath the crust [Cannat, 1996]. Finally, seismic crustal thickness data are restricted to a small number of ridge locations. Gravity data are more widespread, but do not discriminate between crustal thickness variations and lateral variations of the crust and upper mantle density structure. In the following paragraphs, we will keep these limitations in mind, while using gravity-derived crustal thickness, tied to crustal thicknesses determined seismically along two profiles acquired near 66°E

[Minshull *et al.*, 2006; Muller *et al.*, 1999], as a proxy for the ridge's melt supply.

[21] The analysis of seafloor morphology in regions 9 and 10 has revealed large expanses of seafloor with no evidence for a volcanic upper crustal layer (Figure 7). This type of seafloor has been called « smooth seafloor » because it occurs in the form of broad ridges, with a smooth and rounded topography [Cannat *et al.*, 2006]. When sampled by dredging, smooth seafloor domains have yielded serpentinized mantle-derived peridotites, with minor basalts and gabbros [Seyler *et al.*, 2003]. Seafloor with unambiguous volcanic features has also been identified in regions 9 and 10 (Figure 7), as well as corrugated surfaces, similar to those described at faster ridges which are inter-

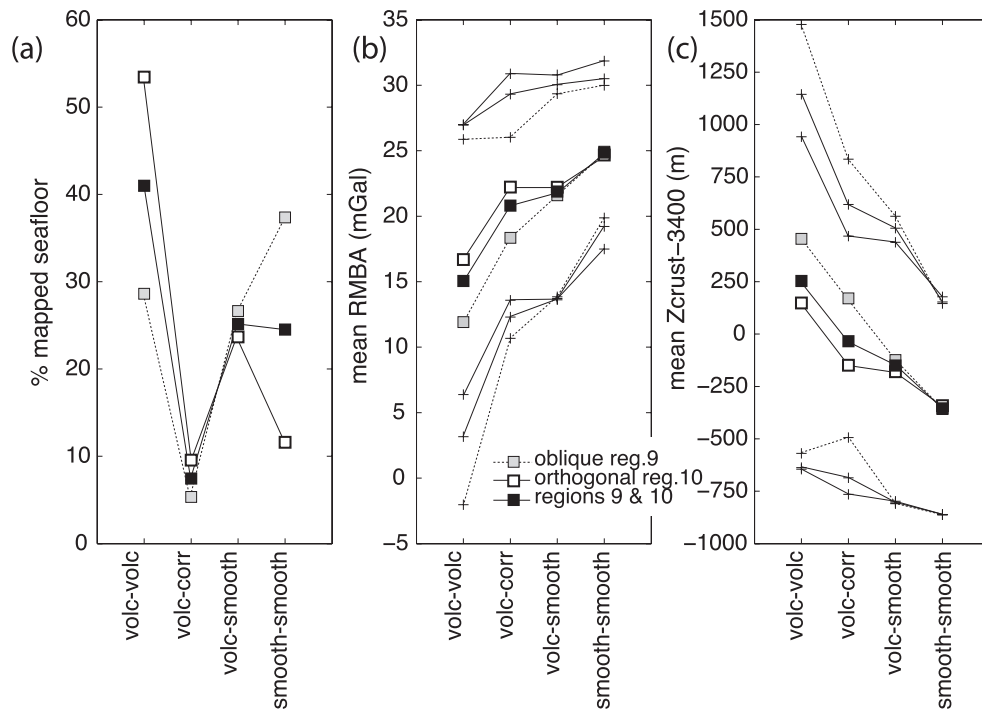


Figure 10. (a) Percent of mapped seafloor, (b) mean RMBA, and (c) mean gravity-derived crustal thickness for conjugate pairs of seafloor morphologies represented in Figure 9 from the time of magnetic anomaly 6 (20 Ma [Cande and Kent, 1995]) to present. Grey squares, oblique ridge region 9; open squares, orthogonal ridge region 10; black squares, both regions. RMBA and gravity-derived crustal thickness from Cannat *et al.* [2006]. Crosses in Figures 10b and 10c correspond to ± 1 standard deviation.

preted as exhumed detachment fault surfaces [Cann *et al.*, 1997; Tucholke *et al.*, 1998]. Smooth seafloor is more abundant (50% of mapped area) and forms flow line-parallel bands in region 9. It is less abundant (28% of mapped area) and forms irregular expanses in region 10 [Cannat *et al.*, 2006].

[22] This contrast between regions 9 and 10 is reinforced if one considers the morphology of conjugate pairs of seafloor domains inferred to have formed simultaneously on each side of the axial valley (Figure 9). Four types of conjugate seafloor morphologies have been recognized (volcanic-volcanic; corrugated-volcanic; smooth-volcanic; and smooth-smooth), and their possible modes of formation have been addressed by Cannat *et al.* [2006]. The smooth-smooth conjugate seafloor morphologies coincide with gravity anomalies which are higher compared to those of other conjugate morphologies. Smooth-smooth conjugates are therefore inferred to form at minimal ridge's melt supply, with no or very little axial volcanism [Cannat *et al.*, 2006]. Figure 10a shows that they are 3 times more common in the oblique-spreading region (9), than in the orthogonal-spreading region

(10). By contrast, the volcanic-volcanic conjugate seafloor morphologies correspond to the lowest gravity anomalies (Figure 10b), suggesting that they are characterized by a thicker crust (Figure 10c). They are nearly twice more common in the orthogonal-spreading region 10, than in the oblique-spreading region 9 (Figure 10a). The volcanic-corrugated and volcanic-smooth conjugate seafloor morphologies have intermediate gravity signatures (Figure 10b). Their respective abundance is similar in the two ridge regions (Figure 10a).

[23] Smooth-smooth conjugate pairs have similar mean gravity signatures in regions 9 and 10 (Figure 10b), suggesting similar mean crustal thickness (~ 400 m less than the reference value of 3.4 km used in the gravity model; Figure 10c). By contrast, volcanic-volcanic and volcanic-corrugated conjugates have significantly lower mean gravity anomaly values in the oblique ridge region 9 (Figure 10b), suggesting higher mean crustal thickness (~ 500 m more than reference value; Figure 10c). The emerging pattern is thus one in which oblique spreading produces larger expanses of avolcanic, or nearly avolcanic, smooth seafloor and lesser expanses of volcanic seafloor. Volcanic

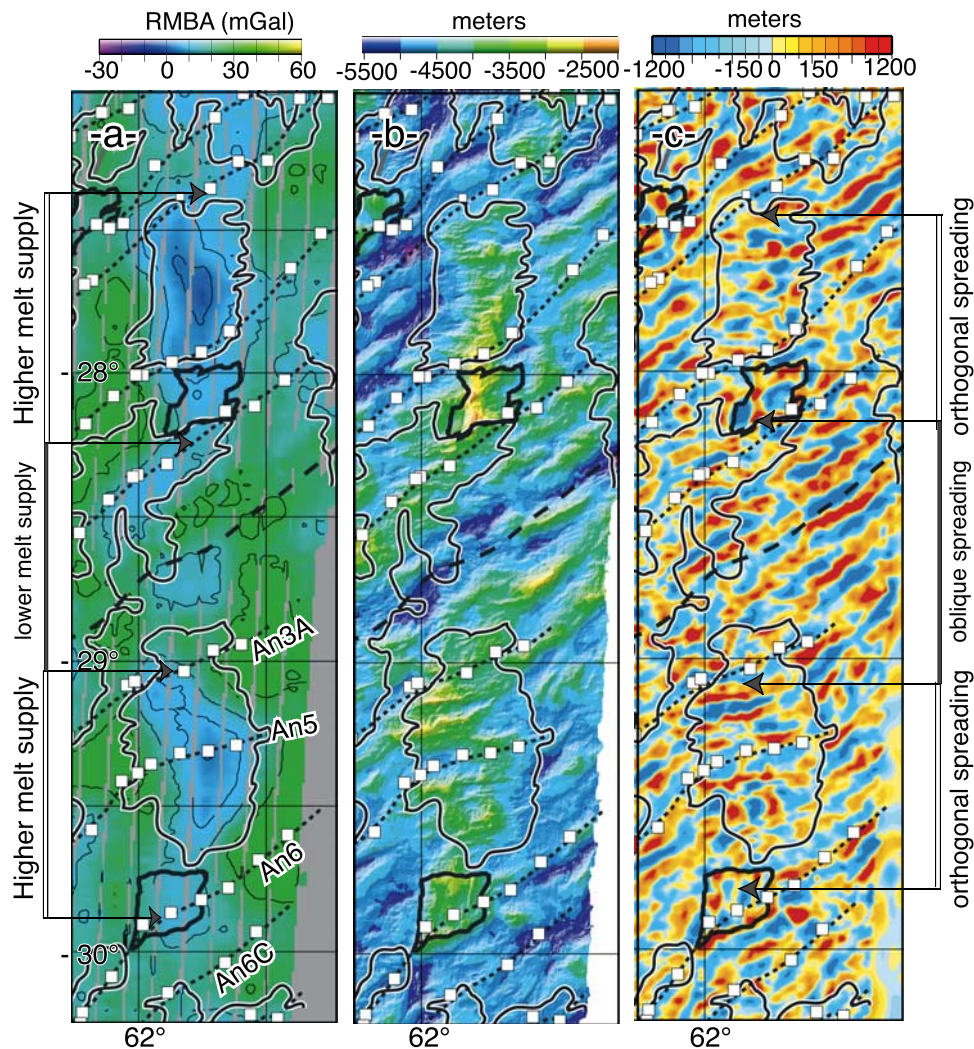


Figure 11. Detailed maps for the area shown as inset in Figure 7. (a) RMBA, (b) seafloor depth, and (c) filtered seafloor depth obtained with GMT fast Fourier transform `grdfft` function, passing wavelength between 5 and 15 km and cosine tapering wavelengths between 2 and 5 km, and between 15 and 20 km. Thick dashed line, Central Magnetic Anomaly; squares, pickings for magnetic anomalies A3A to A6c (corresponding isochrons shown as dashed lines).

seafloor produced in the oblique region has, however, a more negative mean gravity signature (larger crustal thickness and melt supply) than that of the orthogonal region. Therefore, melt distribution appears more focused along axis in the oblique ridge region than in the orthogonal one (Figure 8).

4. Melt Supply and Axial Obliquity Within Oblique Ridge Region 9

[24] Observation of magnetic isochrons in the oblique spreading region 9 (Figure 7) reveals that although the regional obliquity of the ridge (33°; Figure 1) has been maintained over at least the past

26.5 Ma (magnetic anomaly 8), portions of the axis are or have been less oblique over discrete periods. For example, the ridge is presently near orthogonal to spreading over ~50 km in segment 14 (Figure 7). On the basis of the shape of magnetic isochrons, we can also infer that oblique and orthogonal spreading occurred alternatively through time. At the longitude of segment 14, spreading appears to have been oblique prior to the time of magnetic anomaly 5 (Figure 7). At the longitude of segment 13 (Figure 11), spreading was oblique at the times of magnetic anomalies 6 (20 Ma ago), and 3A (5.89 Ma [Cande and Kent, 1995]). In contrast, spreading was nearly orthogonal, over a ~50 km-long portion of the axis, at the time of anomaly 5

(10 Ma). The 14 Ma-long interval between magnetic anomalies 6 and 3A also corresponds, at the longitude of segment 13, to the formation of an elongated gravity low (Figure 11a) and to the emplacement of volcanic seafloor, reflecting enhanced melt supply for this period of time. Magnetic isochrons and gravity data thus suggest that the transition from oblique to orthogonal spreading, then back to oblique spreading, at segment 13 was correlated with enhanced, then reduced melt supply.

[25] Magnetic isochrons can be only drawn for the major magnetic polarity intervals. Using the off-axis seafloor morphology record, we can, however, infer local ridge obliquity and its evolution with a finer temporal resolution. To this aim, we use the orientation of broad tectonic ridges that are prominent in the bathymetry of the smooth seafloor domains (Figure 7). These tectonic ridges are less salient in volcanic seafloor domains, due in part to the superimposition of smaller-scale bathymetric features (scarps and volcanic cones [Cannat *et al.*, 2006]). Filtering the bathymetry for the appropriate wavelengths reveals the lateral continuity and geometry of these structures (Figure 11c), which matches that of magnetic isochrons. Two of these broad ridges, on either sides of the Central Magnetic Anomaly, correspond to the walls of the present-day axial valley (Figures 11b and 11c). We therefore interpret these tectonic ridges as fault blocks, representing former axial valley walls. We use the geometry of these ridges to track past changes in the trend of the axial valley.

[26] Following this approach, we find that the transition from oblique to orthogonal spreading in segment 13 occurred rapidly (within 1 or 2 Ma at the most) just after the time of magnetic anomaly 6 (Figure 11c). This transition appears to have postdated the onset of higher melt supply, as mapped from gravity anomalies (Figure 11a). It occurred during the period of activity of an asymmetric detachment fault, in association with accretion of a corrugated surface to the southern (Antarctic) plate. Similarly, the transition back to oblique spreading occurred rapidly, at the end of the enhanced melt supply episode (as inferred from gravity anomalies in Figure 11a), sometime before magnetic anomaly 3A. It also occurred with the accretion of a corrugated surface (to the northern plate; Figure 11c).

[27] Magnetic, gravity and seafloor morphology data for segment 13, in ridge region 9, therefore suggest that the faults that bound oblique portions

of the axial valley reoriented to spreading-perpendicular within 1 or 2 Ma, during episodes of enhanced melt supply. Incidentally, observations at segment 13 also indicate that rheological and stress conditions in the axial lithosphere during these reorientation events favored the development of corrugated surfaces.

5. Discussion

5.1. Melt Supply and the Proportion of Serpentinized Mantle-Derived Peridotites in the Crust

[28] We have so far used regional axial depths, and seismic and gravity-derived crustal thickness, as proxies for melt supply. However, the two areas we focused on (region 1, and regions 9 and 10) have widespread outcrops of serpentinized mantle-derived peridotites [Dick *et al.*, 2003; Seyler *et al.*, 2003]. At regional scales and for constant mantle temperature, increasing the proportion of variably serpentinized peridotite in the crust will increase the total crustal thickness, and reduce the isostatic axial depth, at constant melt supply and basalt $\text{Na}_{8.0}$. The presence of a significant volume of mantle-derived material in the crust may therefore lead to overestimate melt supply and mantle temperature when using the mean crustal thickness and the mean axial depth proxies. In this section we discuss the impact this could have on our melt supply estimates for regions 1, 9 and 10.

[29] Outcrops of mantle-derived ultramafic rocks are common in the long oblique segment of region 1 [Dick *et al.*, 2003], where we have estimated a melt thickness of about 3.5 km, based on average axial depths. This estimate is at odds with the abundance of ultramafic outcrops [Dick *et al.*, 2003], and it is also much more than predicted for the low ESR of this segment by high mantle viscosity corner flow models [Phipps Morgan *et al.*, 1987; Reid and Jackson, 1981]. Figure 12 shows that maintaining the same mean axial depth for a significantly lower melt supply (configuration B) would be possible, but would require the addition of a significant thickness of nonmagmatic light material to the crust, the most likely candidate being variably serpentinized peridotite. For example, the strong upper mantle cooling configuration B in Figure 12b, which produces only 0.5 km of melt, requires 4.5 km of serpentinized mantle in order to maintain an isostatic depth of 4113 m. If we correct this depth by 600 m for the dynamic effect of axial valley formation (Figure 3),

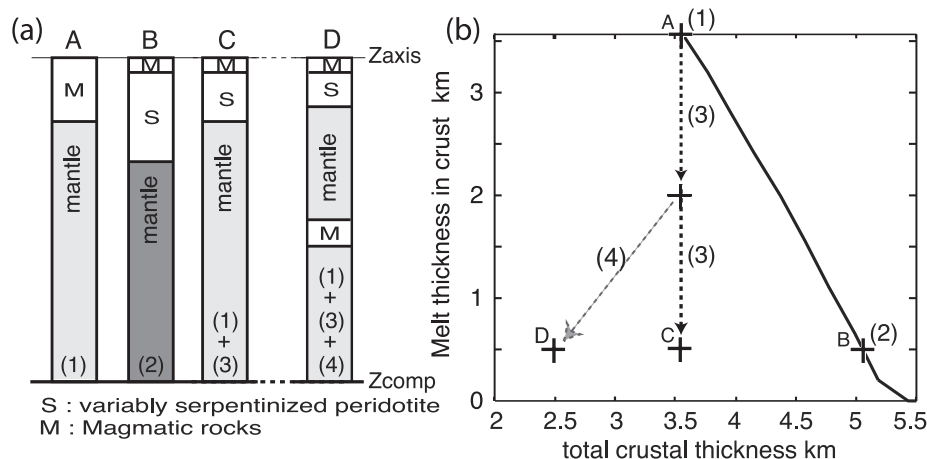


Figure 12. Four crustal and upper mantle configurations (A to D) corresponding to similar isostatic axial depths (Z_{axis} ; compensation depth is Z_{comp} , as in Table 2). These four configurations differ in the amounts of magmatic and partly serpentinized mantle-derived rocks in the crust. Sketches in Figure 12a are not to scale and are generalized, while data points in Figure 12b are calculated for the long oblique ridge segment in region 1. Data points A and B are calculated with our melting model for an ESR of 4 mm a^{-1} , a constant starting mantle temperature of 1350°C , and an isostatic axial depth equal to 4113 m. Data points C and D are calculated with a simple isostatic balance equation. Configuration A corresponds to a fully magmatic crust, with moderate cooling of the mantle from above (process 1). Configuration B corresponds to very pronounced cooling of the mantle from above (process 2). The curve between A and B in Figure 12b shows the effect of increasing upper mantle cooling efficiency at constant ESR. This effect is simulated with enhanced mantle thermal diffusivity (by a factor of 1 for configuration A to 1.7 for configuration B). It is equivalent to going from the *Bown and White* [1994] to the *Reid and Jackson* [1981] model in Figure 5. It results in a decrease of the melt supply and in a progressively cooler and thus denser upper mantle. Isostatic depth is maintained by the addition of a progressively thicker crustal layer of serpentinized peridotite (using density values in Table 2). Total crustal thickness in Figure 12b is the sum of the magmatic component and of this mantle-derived crustal component. Configuration C derives from A, but part of the melt produced has been transported along axis (process 3) out of the area represented. Isostatic depth is maintained with an equivalent thickness of serpentinized peridotite. Finally, configuration D also derives from A, with part of the melt being diverted along axis and another part being trapped in the upper mantle below the crust (process 4; we use an average density of 2900 g cm^{-3} for magmatic rocks in the mantle). Isostatic depth is also maintained with a layer of serpentinized peridotites. Configurations B, C, and D result in large proportions of mantle-derived peridotites in the crust, serpentinization depths being substantially larger in configuration B.

corresponding modeled values are shifted to 1370°C for mantle temperature at 100 km depth, 4.7 km for the melt thickness in configuration A, and 1.4 km in configuration B, with an additional 5 km of serpentinized mantle in the crust. Although there are no seismic data to constrain crustal thickness in this long oblique ridge segment, we view such a thick mantle-derived crustal component as unlikely, simply because it would then be difficult to account for the numerous seismic records of much thinner oceanic crust in other slow and ultraslow settings, and most notably in the easternmost SWIR [Minshull et al., 2006; Muller et al., 1999]. Why would partial serpentinization of the upper mantle be pervasive down to depths of 5 km below seafloor in region 1, when it is not so at depths less than 3 km in these other places? We therefore favor alternative settings such

as configurations C and D in Figure 12, which involve a significant melt production in the sub-axial mantle (process 1), but call for processes such as along-axis melt migration (process 3), and the trapping of some melt in the mantle (process 4), to reduce the amount of melt in the crust of the long oblique segment. In configuration C, melt produced in the mantle has migrated along axis out of the oblique ridge segment and into the adjacent volcanic centers. Given that the oblique segment is very long (184 km), however, melt migration would be expected to be incomplete in its center, leaving a thicker magmatic crust, which is not observed [Dick et al., 2003]. We thus prefer the hybrid configuration D, with a combination of melt migration and melt retention in the mantle beneath the ridge. Finally, one should consider that if mantle cooling from above is intermediate between

A and B, melt migration and melt retention may also operate from the corresponding point on curve A-B, leading to other hybrid configurations, each consistent with the same isostatic axial depth. This illustrates the uncertainty introduced by the serpentinized upper mantle factor for studies of mid-ocean ridge melt supply.

[30] One way to reduce this uncertainty is to focus on areas for which we have good on-axis and off-axis constraints on geology, seafloor morphology, and crustal thickness. This is the case in SWIR regions 9 and 10, for which we have a map of gravity-derived crustal thickness [Cannat *et al.*, 2006], tied to seismic data [Minshull *et al.*, 2006; Muller *et al.*, 1999]. In the following paragraphs, we propose an estimate of the proportion of the crust made of mantle-derived material in these two regions. We do not consider percent serpentinization in this discussion, but simply assume that mantle-derived rocks at different levels in the crust are serpentinized to the right proportion [Miller and Christensen, 1997] to reproduce the velocity-depth gradient modeled from the seismic data by Muller *et al.* [1999] and Minshull *et al.* [2006].

[31] In order to estimate the proportion of the crust made of mantle-derived material in regions 9 and 10, we make the hypothesis that it represents 90% of the crust in smooth seafloor domains. This proportion is consistent with the distribution of rock types in available dredges [Seyler *et al.*, 2003]. We then infer that distal parts of volcanic domains have a transitional crustal architecture, and propose an overall proportion of 20% mantle-derived material in these domains, similar to estimates made for Mid-Atlantic Ridge crust [Cannat *et al.*, 1995]. For corrugated seafloor, we use an intermediate value of 70%.

[32] Given the distribution of each type of seafloor in each region [Cannat *et al.*, 2006], we then use these estimated proportions, and the gravity-derived total crustal thickness (melt plus mantle-derived components), to map the thickness of the mantle-derived crustal component in the two ridge regions, for seafloor ages up to 20 Ma (magnetic anomaly 6; Figure 7). We then subtract the calculated thickness of the mantle-derived crustal component in each ridge region, to the total crustal thickness, and derive the melt thickness supplied to the crust in this region per increment of spreading, averaged over the past 20 Ma. The result is 1.57 km for region 9 (45% of the total mean crustal thickness, 55% of the crust on average being made of mantle-derived residual rocks), and 1.96 km for

region 10 (56% of the total mean crustal thickness, 44% of the crust on average being made of mantle-derived residual rocks). The proportions used for mantle-derived material in smooth, volcanic and corrugated seafloor domains, and therefore these estimated melt supply values, have significant uncertainties. They suggest a time-integrated contrast in melt supply between the two regions of about 0.4 km in melt thickness, similar to the present-day difference in melt supply inferred from contrasted regional axial depths (Figure 6) and basalt sodium contents. This contrast would not be visible in the off-axis topographic and gravity records (Figure 8) because it is compensated by a greater proportion of serpentinized mantle rocks in region 9.

[33] We now use the same melting and isostatic compensation model as in Figures 4 to 6, to predict isostatic depths from the mean melt thickness and for the proportion of crustal mantle-derived rocks estimated above for regions 9 and 10 (Figure 13a). To do so, we make the hypothesis that no melt remains trapped in the upper mantle. If this is wrong (configuration D in Figure 12), or if we have underestimated the melt component in the crust, our predicted axial depths should be too deep. We calculate an isostatic depth of 4599 m for region 9 (melt thickness: 1.57 km; mantle-derived crustal component: 55%), and of 4493 m for region 10 (melt thickness: 1.96 km; mantle-derived crustal component: 44%). These results provide a better fit to measured regional axial depths (Table 1), than the depth values predicted for a 3.5 km-thick, entirely magmatic crust in Figure 6. Yet they are significantly deeper than regional axial depths corrected for the probable dynamic contribution of the axial valley (about 600 m; Figure 3). $\text{Na}_{8,0}$ melt values calculated for these estimated melt thicknesses, and an initial mantle sodium content of 0.27 wt%, are higher (4.57 and 4.34 wt% respectively for regions 9 and 10) than measured values (Table 1). These measured values are, however, well modeled using an initial mantle sodium content of 0.23 wt% (Figure 13b). Given the large uncertainties attached to the melting model, we do not consider this a reliable indication on mantle compositions in the area. Instead, deeper calculated depths and higher basalt sodium contents could point to an intermediate crustal and upper mantle configuration for regions 9 and 10, with a higher melt supply, but with some melt retention in the mantle (configuration D in Figure 12). Whatever the case, measured regional axial depths and $\text{Na}_{8,0}$ contents of basalts from regions 9 and 10 of the SWIR do not appear

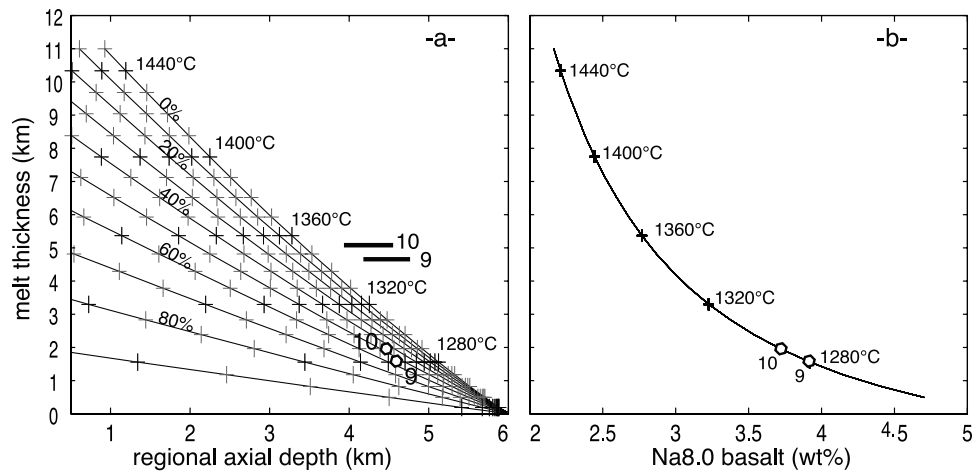


Figure 13. Melt supply (thickness of melt produced per increment of plate separation) calculated as a function of (a) isostatic regional axial depth and (b) basalt Na_{8,0} content for initial mantle temperatures ranging between 1250°C and 1450°C at a depth of 100 km, an ESR value of 7 mm a⁻¹, and varying proportions (0 to 90%) of mantle-derived peridotites in the crust. Our estimates of the melt thickness and of the proportion of mantle-derived material in the crust of regions 9 and 10 (see text) are plotted in this diagram. An ESR of 6 mm a⁻¹ (region 9) yields similar curves, shifted to the bottom right of the diagram as in Figure 6 by about the distance between data points for regions 9 and 10. These data points correspond to predicted isostatic axial depths that are roughly consistent with the mean axial depth in each region (shown as bold lines, the right end to actual average depths and the left end to depths corrected for the possible dynamic contribution of the axial valley; Figure 3). The melt thickness versus basalt Na_{8,0} curve in Figure 13b is calculated for an initial mantle sodium content of 0.23 wt%.

inconsistent with the presence of large proportions of mantle-derived material in the crust.

5.2. Spreading Rate, Spreading Obliquity, and Melt Production in the Subaxial Mantle

[34] Large-scale variations of melt supply along the SWIR, as inferred from regional axial depths and basalt sodium contents in Figure 1, appear primarily associated with the Marion-Crozet-Kerguelen geoid high. They can be modeled with large-scale variations in mantle temperature (Figures 4 and 6), but could also be associated with compositional heterogeneities. In any case, they largely obscure the effect of ridge obliquity on melt supply.

[35] Changes in spreading obliquity along the SWIR correspond to changes in effective half-spreading rates between 4 and 7 mm a⁻¹ (Figure 2), well within the critical range for most mantle melting models [see White *et al.*, 2001, Figure 24]. Figure 14 shows two end-member models in terms of the relationship between spreading rate and melt production: one (Figure 14a) is sketched after the Bown and White [1994] model of corner flow with a spreading-rate dependant lithosphere wedge angle; the other (Figure 14b) is sketched after the corner flow model of Reid and Jackson [1981], and is analogous to the Phipps

Morgan *et al.* [1987] model favored by Dick *et al.* [2003]. The difference between these two end-member models is that in Figure 14a, mantle upwelling is focused, and therefore accelerated, beneath the ridge, while in Figure 14b, mantle upwelling velocity is nearly equal to the effective spreading rate. As discussed by White *et al.* [2001], there are two principal ways to focus mantle upwelling beneath the ridge: one is to increase the lithosphere wedge angle as spreading-rate decreases [Bown and White, 1994; Spiegelman and McKenzie, 1987], which could happen if cooling with age and/or melt migration produce sharp lateral viscosity contrasts in the subaxial mantle; the other is to introduce a component of buoyant (i.e., active) upwelling [Scott, 1992; Sotin and Parmentier, 1989].

[36] ESR and estimated melt thicknesses values proposed in this paper for three representative regions of the SWIR are also plotted on Figure 14, as well as a global compilation of oceanic seismic crustal thickness [Bown and White, 1994], and more recent seismic crustal thickness determinations for the SWIR [Muller *et al.*, 1999], and for Gakkal Ridge [Jokat *et al.*, 2003]. Our first comment is that the two end-member models in Figure 14 predict similar changes in melt thickness

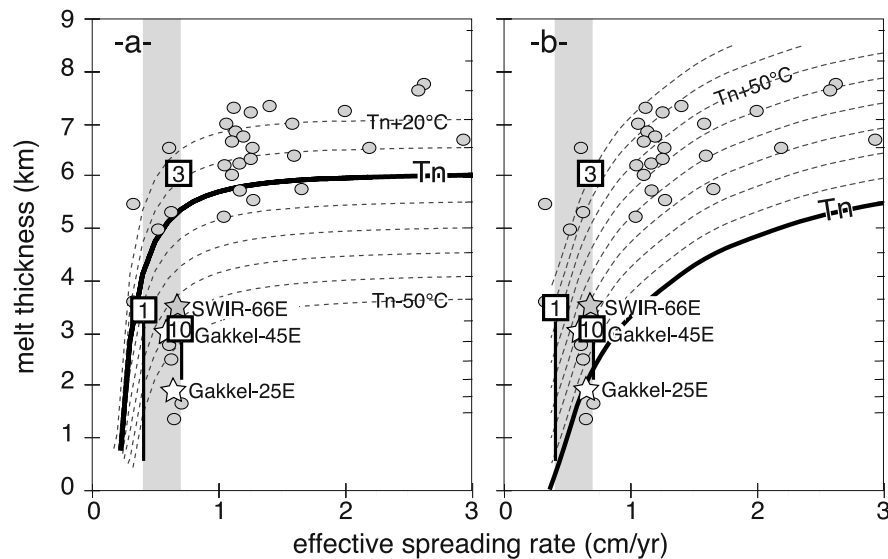


Figure 14. Sketches showing two end-member models for the relationship between melt supply and ESR (equal to half-spreading rate for orthogonal spreading ridges). Shaded domains show the range of ESR along the SWIR (Figure 2). Melt supply at SWIR regions 1, 3, and 10 (open squares) is expressed as the thickness of melt produced per increment of spreading, as inferred in Figure 6. Vertical lines for regions 1 and 10 indicate the range of alternative melt supply estimates discussed in text. Grey star is seismic crustal thickness average at the SWIR near 66°E [Muller *et al.*, 1999]. Open stars are seismic crustal thickness averages in the eastern part of Gakkel Ridge [Jokat *et al.*, 2003]. Grey dots are a global compilation of seismic crustal thickness in slow-spread oceans [Bown and White, 1994]. In Figure 14a (sketch after Bown and White [1994]), melt thickness remains unaffected down to very slow ESR, at which point it decreases abruptly. In Figure 14b (sketch after Reid and Jackson [1981]), melt thickness decreases gradually at ESR less than 3 cm a^{-1} . Bold curves correspond to “normal mantle temperature” (T_n) (corresponding to the production of a melt thickness of 6 km in adiabatic conditions).

for two SWIR regions of contrasted obliquity: about 1.5 km more melt for an ESR variation of 4 to 7 mm a^{-1} (Figure 14). This is consistent with our estimate of the difference in melt supply between regions 1 and 2 (section 3 of this paper). The two models differ widely, however, in their prediction of the total melt thickness deficit owing to nonadiabatic mantle cooling at slow ESRs. For a normal temperature mantle and an ESR of 4 mm a^{-1} , this predicted deficit is of about 2 km in the focused mantle upwelling model (Figure 14a), and of about 5 km in the unfocused mantle upwelling model (Figure 14b).

[37] The unfocused mantle upwelling model predicts that ridge region 3, which is representative of the high melt supply regions in the central SWIR (Figure 1), has a very hot (and/or extremely fertile) mantle, while region 10, in the eastern SWIR, would have nearly “normal” mantle temperatures (Figure 14b). This would indicate a very broad zone of influence of the Marion-Crozet plume material along the ridge, which is inconsistent with the other geophysical [Georgen *et al.*, 2001] and geochemical [Meyzen *et al.*, 2005] studies of the

involvement of plume material in this part of the SWIR. As already shown by [White *et al.*, 2001], the unfocused mantle upwelling model also predicts anomalously high mantle temperatures for the global compilation of seismic crustal thicknesses determined at slow spreading oceanic ridges (Figure 14b). We therefore favor the alternative, focused mantle upwelling model (Figure 14a).

[38] In this model, the central SWIR regions have nearly “normal” to slightly elevated mantle temperatures, and thin crust in the eastern regions of the SWIR and at Gakkel Ridge is primarily caused by low initial mantle temperatures. This would fit with the anomalously low upper mantle seismic velocities determined in tomographic models of the eastern SWIR [Debaille *et al.*, 2005; Debaille and L  v  que, 1997]. The long oblique segment in ridge region 1 in the western SWIR [Dick *et al.*, 2003] presents a complex case. Regional axial depth there suggests an intermediate melt supply, consistent with the focused flow model at near-normal mantle temperatures (Figure 14a). Yet geological observations show that the crust in this oblique ridge

segment is nearly amagmatic, being mostly made of mantle-derived ultramafic rocks [Dick *et al.*, 2003]. In Figure 12, we have proposed two crustal and upper mantle configurations which may explain this paradox. In configuration C, melt produced in the mantle migrated along axis out of the oblique ridge segment and into the adjacent volcanic centers. In configuration D, which we favor, along-axis melt migration is complemented by melt trapping in the mantle. In the next section, we will argue that ridge obliquity can have a significant impact on these two processes.

5.3. Melt Distribution and Ridge Obliquity at Segment Scale

[39] We have shown in Figure 11 that localized events of enhanced melt supply in the oblique SWIR region 9, coincide in time and space with a reorientation of the ridge from oblique to orthogonal to spreading. This observation can lead to two opposite interpretations. In one interpretation, ridge reorientation precedes and causes the increase in melt supply because it results in a faster ESR. A delay should then be observed between ridge reorientation and the formation of a thicker volcanic crust. This delay is needed for the faster ESR to modify the thermal structure of the uppermost mantle, allowing melting to proceed to shallower depths. In the other interpretation, higher melt supply causes ridge reorientation because it modifies the rheology of the axial lithosphere, allowing the axial valley bounding faults to reorient to orthogonal (Figure 15). We favor this second interpretation, because we see no evidence in our bathymetry and gravity data for a delay between ridge reorientation and the formation of thicker volcanic crust. Furthermore, both end-member melting models in Figure 14 predict that ESR variations between oblique and orthogonal sections of ridge region 9 (5.9 to 7 mm a^{-1}) would cause only a limited change in melt supply (about 0.5 km).

[40] Temperature is the main factor controlling rheology in the oceanic lithosphere, and melt advection is the most efficient way to provide heat to mid ocean ridges [e.g., Sleep, 1975]. We thus propose that enhanced melt supply events at an oblique ridge lead to rapid ridge reorientation because large volumes of melt are transported through the lithospheric mantle and through the crust in dikes that form perpendicularly to the direction of least compressive stress (Figure 15). This would create a hot orthogonal zone of weakness in the axial lithosphere and promote the

formation of orthogonal axial valley bounding faults (Figure 15). Dikes, rooting in magma-rich regions at the base of the axial lithosphere, have already been proposed as the dominant mode of melt transport to the prominent volcanic centers observed at the SWIR [Cannat *et al.*, 1999; Dick, 1989]. TOBI side scan sonar exploration has also documented many smaller spreading-perpendicular volcanic ridges in oblique portions of SWIR regions 7 and 8 [Sauter *et al.*, 2002]. Observations in Iceland and Ethiopia indicate that individual dikes cutting through the lithosphere and extending tens of kilometers along the rift zone can be emplaced in a matter of weeks [Arnadottir *et al.*, 1998; Wright *et al.*, 2006], while swarms of such dikes may be emplaced at a given location over periods of a few years [Tryggvason, 1994]. We propose that the emplacement of dike swarms at ultraslow spreading ridges may occur over similar timescales.

[41] In our interpretation, avolcanic or nearly avolcanic sections of the ridge represent the most distal parts of the crustal melt distribution system, out of the reach of most dikes that root in centers of enhanced melt supply (Figure 15). The resulting segmentation pattern, with prominent volcanic centers and long intervening melt-poor ridge sections, is not specific to oblique ridge regions: region 10 of the SWIR, and the eastern Gakkal Ridge [Michael *et al.*, 2003], are orthogonal to spreading and present these same characteristics. Spreading obliquity, however, clearly leads to more focused volcanism: volcanic centers in the orthogonal ridge region 10 are surrounded by wider expanses of volcanic terrains, while the oblique region 9 displays a larger proportion of avolcanic or nearly avolcanic smooth terrains [Cannat *et al.*, 2006]. In Figure 15, the lateral extent of volcanic domains is controlled by dike emplacement and lateral propagation, as previously suggested by Cannat *et al.* [2006]. Individual diking events are expected to respond to magmatic overpressure, and to the stress distribution in the lithosphere [Behn *et al.*, 2006a; Rubin, 1995]. We propose that dike swarms feeding eruptions at the seafloor in oblique ridge regions should also be collectively limited by the spreading-perpendicular width of the regional lithospheric weakness zone (Figure 15).

[42] Another aspect of this dike-controlled melt distribution model, is that portions of the ridge that do receive some melt, but not enough to build sufficient magmatic overpressure and open a dike conduit through the thick axial lithosphere, are

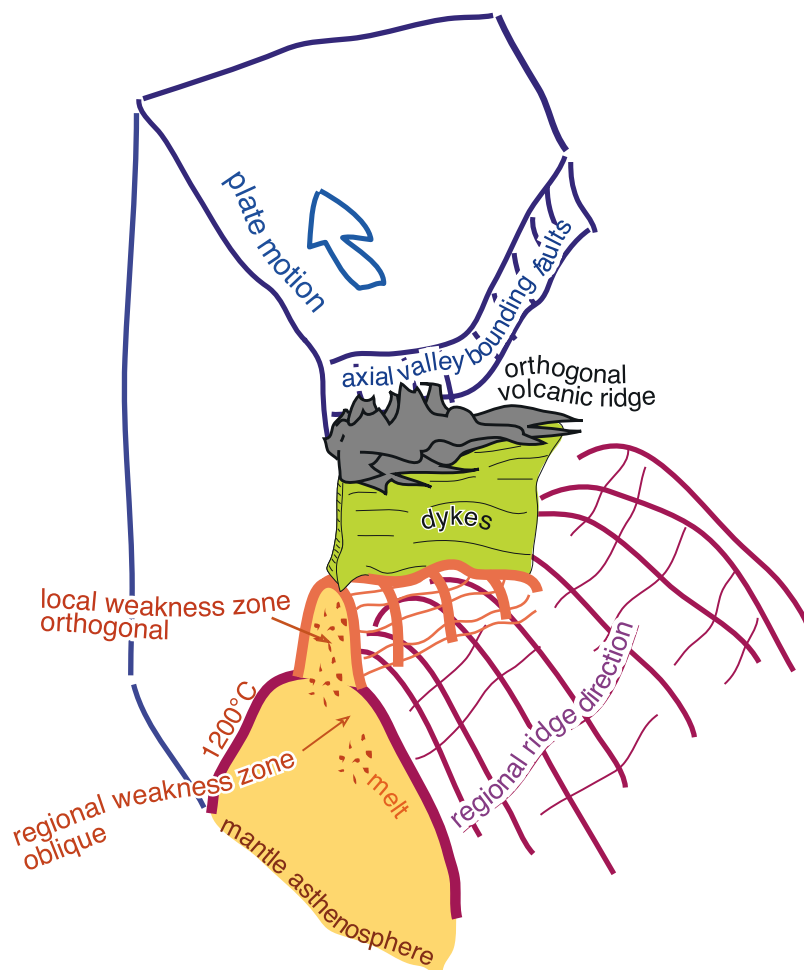


Figure 15. Sketch of an oblique-spreading ultraslow ridge. Only one lithospheric plate is shown in order to view the lithosphere-asthenosphere boundary (assumed to lie close to the 1200°C isotherm). Owing to mantle upflow and melt migration, this boundary shallows in the axial region, forming a weakness zone that guides axial valley bounding faults. This regional weakness zone (or asthenospheric channel) has an oblique trend at scales greater than 100 km. We propose that repeated dike injections feed orthogonal volcanic ridges in areas of high melt supply. These injections heat the mantle lithosphere, forming local and shallower weakness zones, also orthogonal to spreading. Axial valley bounding faults reorient, following these local weakness zones. The typical dimension for orthogonal sections in oblique regions of the SWIR is 40 to 50 km (Figure 16). We propose that dike propagation in these oblique ridge regions is limited by the width of the regional lithospheric weakness zone in the direction orthogonal to spreading.

more likely to develop the architecture sketched as configuration D in Figure 12, with significant along-axis melt migration, and trapped melt in the lithospheric mantle. This may be the case beneath the long avolcanic sections of the ridge in regions 9 and 10, and also beneath the long oblique segment in region 1.

[43] Orthogonal volcanic sections in oblique regions of the SWIR are typically 40 to 50 km-long (Figure 16), and are separated by oblique and melt-starved ridge sections that extend up to 80 km in the direction orthogonal to spreading [Dick *et al.*, 2003]. These oblique sections of the ridge have

first been described as long nontransform discontinuities [Mendel *et al.*, 1997; Rommevaux-Jestin *et al.*, 1997] in reference to substantially shorter features of the faster Mid-Atlantic Ridge [Grindlay *et al.*, 1991], then as amagmatic ridge segments [Dick *et al.*, 2003]. The ridge segment nomenclature used in Figures 7, 11 and 16 [Cannat *et al.*, 1999] follows the earlier definition. For example, in Figure 16, we identify sigmoidal-shaped segments that include about half of the deeper oblique ridge sections at each end of the orthogonal volcanic sections, in much the same way as segments of the Mid-Atlantic Ridge include a melt-rich

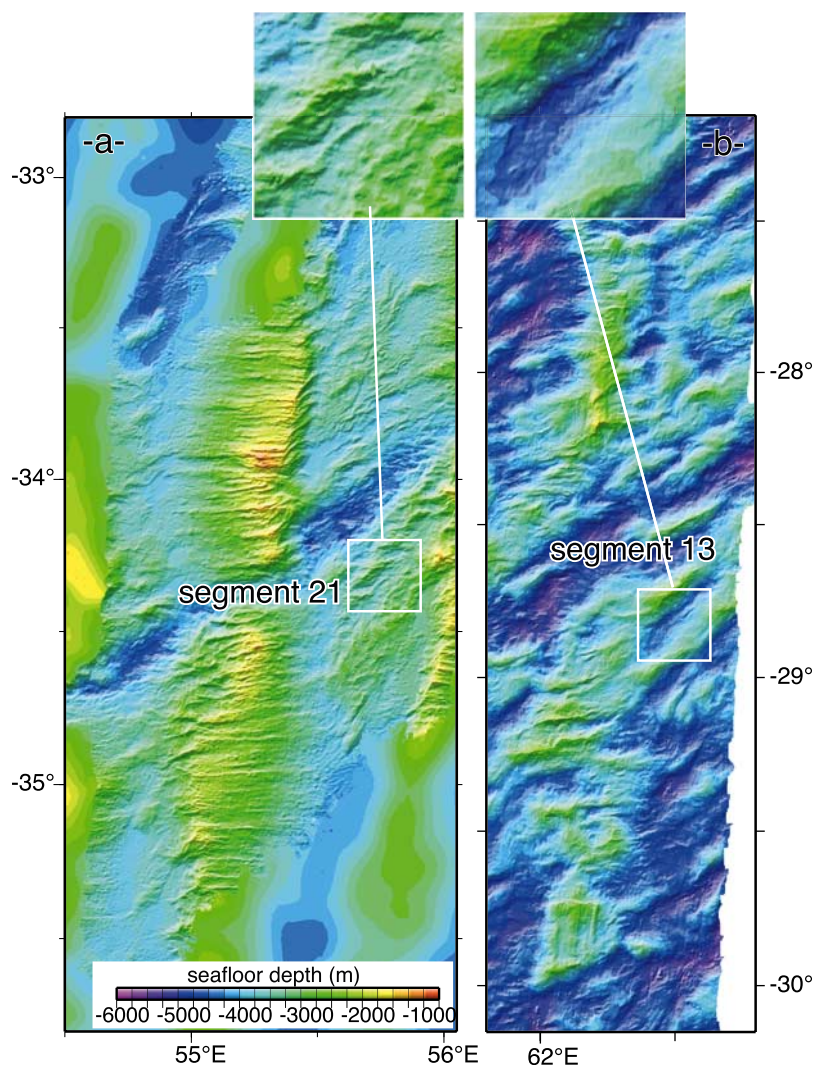


Figure 16. The segmentation pattern in two oblique regions of the SWIR. Bathymetric maps, same spatial and color scales. (a) Ridge segment 21 in region 7 (bathymetry from *Mendel et al.* [2003]; satellite-derived topography [*Smith and Sandwell*, 1997]) is shown in areas not covered by shipboard bathymetry) and (b) ridge segment 13 in region 9 (same area as in Figure 11). The mean axial depth in region 7 is ~ 700 m shallower than in region 9 (Table 1), yielding an estimated 1 km increase in melt thickness (Figure 6). Both maps extend off axis to crustal ages of about 24 Ma. In Figure 16a, ridge orthogonality and significant volcanic activity have been maintained over at least the past 20 Ma. In Figure 16b, volcanic activity has been transient and associated with equally transient episodes of orthogonal spreading (Figure 11). Insets show details of seafloor morphologies formed in the oblique ridge sections of both regions: in Figure 16a they display occasional volcanic cones and patterns of NE and EW trending scarps which suggest complex interplays between spreading-perpendicular extension and transform tectonics; by contrast, in Figure 16b, oblique sections display the characteristic features of the smooth seafloor terrains (broad ridge parallel ridges and lack of scarps and volcanic cones [*Cannat et al.*, 2006]).

segment center, and the deeper nodal basins at each end. *Baines et al.* [2007] propose an alternative nomenclature for the area of Figure 16a, in line with the work of *Dick et al.* [2003], that identifies these oblique sections, and the intervening orthogonal section as separate segments (numbered GA-2ob, GA-3, and GA-4ob). We favor the earlier definition of a segment because our melt distribu-

tion model does not view oblique sections of the ridge as independent entities. Instead, we call for along-axis melt migration at depth toward the orthogonal volcanic sections, and for melt redistribution by dikes that propagate at shallower depths from the volcanic centers, toward the oblique sections. However, this definition of a segment shows its limits in the case of the very long oblique

section in SWIR region 1. It is so long (184 km) that it almost qualifies as a ridge region of its own, and that it is not likely that its central part exchanges large volumes of melt with the Joseph Mayes or Narrowgate volcanic centers, each more than 90 km away. In addition, ESR variations between oblique and orthogonal sections of ridge region 1 (3.8 to 7 mm a⁻¹) are high enough to cause significant changes in mantle melting and melt supply (about 1.5 km). We would nonetheless argue that our model of dike propagation, melt migration at depth, and melt trapping in the sub-axial mantle is pertinent to study the characteristics of this oblique super-segment. In particular, its axial lithosphere is probably very thick [Behn *et al.*, 2006b]. In this context, it could be that dikes feeding eruptions are uncommon because exceptionally large volumes of melt are required to build sufficient overpressure. This would impede the formation of orthogonal volcanic centers, and favor melt trapping in the mantle.

6. Principal Conclusions

[44] The SWIR presents large-scale (>200 km) variations in axial depths and basalt sodium contents that are consistent with along-axis variations in melt supply from probably less than 3 km of melt per increment of plate separation in the easternmost SWIR, to probably more than 6 km at the longitude of Crozet and Marion Islands. These large-scale variations are associated with the Marion-Crozet-Kerguelen geoid high (Figure 1c) and appear primarily owing to heterogeneities in mantle temperature, possibly with the additional effect of mantle compositional heterogeneities. These large-scale heterogeneities of the mantle source largely obscure the effect of along-axis changes in ridge obliquity.

[45] Focusing on adjacent ridge regions, we have, however, been able to show that the maximum range of effective spreading rates (ESR), associated with the transition from orthogonal to oblique spreading along the SWIR (from about 4 mm a⁻¹ to about 7 mm a⁻¹), corresponds to changes in melt thickness of the order of 1.5 km, for constant initial temperature and composition of the mantle source. This effect is significant, but not enough to produce near-amagmatic spreading in the most oblique regions of the ridge, as proposed by Dick *et al.* [2003], unless associated with an anomalously cold and/or depleted mantle source.

[46] We also find that the melt deficit for an ESR of 4 mm a⁻¹, with respect to adiabatic mantle melting, is probably only of the order of 2 km, for a mantle source of normal temperature. This is much less than the prediction of models with corner flow of a high-viscosity mantle [Phipps Morgan *et al.*, 1987; Reid and Jackson, 1981], in which slow upwelling velocities allow pronounced cooling of the mantle. We therefore support the conclusion of White *et al.* [2001] that mantle upwelling beneath slow and ultraslow ridges is somewhat focused and accelerated, thereby reducing the effect of slow spreading rates and ridge obliquity on upper mantle cooling and the subsequent reduction of melt supply.

[47] Faced with the paradox that very oblique SWIR regions do not appear to have near-zero melt supply, but show large outcrops of mantle-derived ultramafic rocks, and in many cases, no evidence for axial volcanism [Cannat *et al.*, 2006; Dick *et al.*, 2003], we develop a model in which some of the melt produced in the mantle beneath these oblique regions migrates along axis to more volcanically robust areas, another part is trapped in the lithospheric mantle of these oblique ridge sections, and only a small amount makes it to the seafloor as lavas or shallow intrusives.

[48] We also observe that enhanced melt supply events in oblique sections of the ridge lead to a rapid reorientation of the ridge from oblique to orthogonal to spreading. We propose that this is due to rapid melt transport in dikes that form perpendicularly to the direction of least compressive stress (Figure 15), and create a hot orthogonal zone of weakness in the axial lithosphere. Avolcanic sections of the ridge represent the most distal parts of this crustal melt redistribution system. The resulting segmentation pattern, with prominent volcanic centers and long intervening melt-poor ridge sections, is not specific to oblique ridge regions. Obliquity does, however, appear to limit the lateral extension of volcanic centers, and to favor the formation of large expanses of avolcanic seafloor. We propose that this occurs via two combined effects: one is that lateral dike propagation may be limited in oblique ridge sections by the width of the axial lithospheric weakness zone, or lithospheric channel (Figure 15), and the other is that large obliquity probably means a thick axial lithosphere [Behn *et al.*, 2006b], which may impede dike formation unless large volumes of melt can gather and build sufficient overpressure.

Acknowledgments

[49] This work is largely based on a set of data acquired during the SWIR 61-65 cruise on R/V *Marion Dufresne* in 2003 and was supported by the Dyeti Program of CNRS-INSU. Maps were drawn with the GMT software [Wessel and Smith, 1995]. We thank our G-Cubed editor and our three anonymous reviewers for very helpful comments and are grateful to many colleagues, particularly to Henry Dick, Laurent Montesi, Luc Lavier, and Javier Escartin for discussions which helped us through this work. This is IGP contribution 2271.

References

- Arnadottir, T., F. Sigmundsson, and P. T. Delaney (1998), Sources of crustal deformation associated with the Krafla, Iceland, eruption of September 1984, *Geophys. Res. Lett.*, *25*(7), 1043–1046.
- Baines, A. G., M. J. Cheadle, H. J. B. Dick, A. H. Scheirer, B. E. John, N. J. Kusznir, and T. Matsumoto (2007), Evolution of the Southwest Indian Ridge from 55°45'E to 62°E: Changes in plate-boundary geometry since 26 Ma, *Geochem. Geophys. Geosyst.*, *8*, Q06022, doi:10.1029/2006GC001559.
- Behn, M. D., W. R. Buck, and I. S. Sacks (2006a), Topographic controls on dike injection in volcanic rift zones, *Earth Planet. Sci. Lett.*, *246*(3–4), 188–196.
- Behn, M. D., L. Montesi, and J. L. Barry (2006b), Effect of spreading rate and obliquity on mantle melting: Insight from scaling relations and numerical models, *Eos Trans. AGU*, *85*(52), Abstract VG11-03.
- Bown, J. W., and R. S. White (1994), Variation with spreading rate of oceanic crustal thickness and geochemistry, *Earth Planet. Sci. Lett.*, *121*, 435–449.
- Cande, S. C., and D. V. Kent (1995), Revised calibration of the geomagnetic polarity timescale for the Late Cretaceous and the Cenozoic, *J. Geophys. Res.*, *100*, 6093–6095.
- Cann, J. R., D. K. Blackman, D. K. Smith, E. McAllister, B. Janssen, S. Mello, E. Avgerinos, A. R. Pascoe, and J. Escartin (1997), Corrugated slip surfaces formed at North Atlantic ridge-transform intersections, *Nature*, *385*, 329–332.
- Cannat, M. (1996), How thick is the magmatic crust at slow spreading oceanic ridges?, *J. Geophys. Res.*, *101*(B2), 2847–2857.
- Cannat, M., et al. (1995), Thin crust, ultramafic exposures, and rugged faulting patterns at the Mid-Atlantic Ridge (22°–24°N), *Geology*, *23*(1), 49–52.
- Cannat, M., C. Rommevaux-Jestin, D. Sauter, C. Deplus, and V. Mendel (1999), Formation of the axial relief at the very slow spreading Southwest Indian Ridge (49°–69°E), *J. Geophys. Res.*, *104*(B10), 22,825–22,843.
- Cannat, M., C. Rommevaux-Jestin, and H. Fujimoto (2003), Melt supply variations to a magma-poor ultra-slow spreading ridge (Southwest Indian Ridge 61° to 69°E), *Geochem. Geophys. Geosyst.*, *4*(8), 9104, doi:10.1029/2002GC000480.
- Cannat, M., J. R. Cann, and J. MacLennan (2004), Some hard rock constraints on the heat supply to mid-ocean ridges, in *Mid-Ocean Ridges: Hydrothermal Interactions Between the Lithosphere and Oceans*, *Geophys. Monogr. Ser.*, vol. 148, edited by C. German, J. Lin, and L. Parson, pp. 111–150, AGU, Washington, D. C.
- Cannat, M., D. Sauter, V. Mendel, E. Ruellan, K. Okino, J. Escartin, V. Comber, and M. Baala (2006), Modes of seafloor generation at a melt-poor ultra-slow-spreading ridge, *Geology*, *34*(7), 605–608.
- Debayle, E., and J. J. Lévêque (1997), Upper mantle heterogeneities in the Indian Ocean from wave form inversion, *Geophys. Res. Lett.*, *24*, 245–248.
- Debayle, E., B. Kennett, and K. Priestley (2005), Global azimuthal seismic anisotropy and the unique plate-motion deformation of Australia, *Nature*, *433*(7025), 509–512.
- DeMets, C., R. G. Gordon, D. F. Argus, and S. Stein (1994), Effect of recent revisions to the geomagnetic reversal time scale on estimates of current plate motions, *Geophys. Res. Lett.*, *21*(20), 2191–2194.
- Dick, H. J. B. (1989), Abyssal peridotites, very slow spreading ridges and ocean ridge magmatism, in *Magmatism in the Ocean Basins*, edited by A. D. Saunders, and M. J. Norry, *Geol. Soc. Spec. Publ.*, *42*, 71–105.
- Dick, H. J. B., P. S. Meyer, S. Bloomer, S. Kirby, D. Stakes, and C. Mawer (1991), Lithostratigraphic evolution of an *in-situ* section of oceanic layer 3, *Proc. Ocean Drill. Program Sci. Results*, *118*, 439–538.
- Dick, H. J. B., J. Lin, and H. Schouten (2003), An ultraslow-spreading class of ocean ridge, *Nature*, *426*, 405–412.
- Georgen, J. E., J. Lin, and H. J. B. Dick (2001), Evidence from gravity anomalies for interactions of the Marion and Bouvet hotspots with the Southwest Indian Ridge: Effects of transform offsets, *Earth Planet. Sci. Lett.*, *187*, 283–300.
- Grindlay, N. R., P. J. Fox, and K. C. MacDonald (1991), Second-order axis discontinuities in the South Atlantic: Morphology, structure, and evolution, *Mar. Geophys. Res.*, *13*, 21–50.
- Grindlay, N. R., J. A. Madsen, C. Rommevaux, and J. Sclater (1998), A different pattern of ridge segmentation and mantle Bouguer gravity anomalies along the ultra-slow spreading Southwest Indian Ridge (15°30'E to 25°E), *Earth Planet. Sci. Lett.*, *161*, 243–253.
- Horner-Johnson, B. C., R. G. Gordon, S. M. Cowles, and D. F. Argus (2005), The angular velocity of Nubia relative to Somalia and the location of the Nubia-Somalia-Antarctica triple junction, *Geophys. J. Int.*, *162*(1), 221–238.
- Johnson, K. T. M., and H. J. B. Dick (1992), Open system melting and temporal and spatial variation of abyssal peridotite and basalt at the Atlantis II Fracture Zone, *J. Geophys. Res.*, *97*, 9219–9242.
- Jokat, W., O. Ritzmann, M. C. Schmidt-Aursch, S. Drachev, S. Gauger, and J. Snow (2003), Geophysical evidence for reduced melt production on the Arctic ultraslow Gakkel mid-ocean ridge, *Nature*, *423*, 962–965.
- Klein, E. M., and C. H. Langmuir (1987), Global correlations of ocean ridge basalt chemistry with axial depth and crustal chemistry, *J. Geophys. Res.*, *92*, 8089–8115.
- Langmuir, C. H., E. M. Klein, and T. Plank (1992), Petrological systematics of mid-ocean ridge basalts: Constraints on melt generation beneath ocean ridges, in *Mantle Flow and Melt Generation at Mid-Ocean Ridges*, *Geophys. Monogr. Ser.*, vol. 71, edited by J. Phipps Morgan, D. K. Blackman, and J. M. Sinton, pp. 183–280, AGU, Washington, D. C.
- le Roex, A. P., H. J. B. Dick, and R. T. Watkins (1992), Petrogenesis of anomalous K-enriched MORB from the Southwest Indian Ridge: 11°53' to 14°38'E, *Contrib. Mineral. Petrol.*, *110*, 253–268.
- Lehnert, K., Y. Su, C. H. Langmuir, B. Sarbas, and U. Nohl (2000), A global geochemical database structure for rocks, *Geochem. Geophys. Geosyst.*, *1*(5), doi:10.1029/1999GC000026.
- Lin, J., G. M. Purdy, H. Schouten, J. C. Sempere, and C. Zervas (1990), Evidence from gravity data for focused magmatic accretion along the Mid-Atlantic Ridge, *Nature*, *344*, 627–632.

- Magde, L. S., and D. W. Sparks (1997), Three-dimensional mantle upwelling, melt generation, and melt migration beneath segments of slow spreading ridges, *J. Geophys. Res.*, *102*(B9), 20,571–20,583.
- Mahoney, J., A. P. le Roex, Z. Peng, R. L. Fisher, and J. H. Natland (1992), Southwestern limits of Indian Ocean Ridge mantle and the origin of low $^{206}\text{Pb}/^{204}\text{Pb}$ mid-ocean ridge basalt: Isotope systematics of the central southwestern Indian Ridge, *J. Geophys. Res.*, *97*, 19,771–19,790.
- McKenzie, D. (1984), The generation and compaction of partially molten rock, *J. Petrol.*, *25*(3), 713–765.
- Mendel, V., D. Sauter, L. Parson, and J.-R. Vanney (1997), Segmentation and morphotectonic variations along a super-slow spreading center: The Southwest Indian Ridge (57°E–70°E), *Mar. Geophys. Res.*, *19*, 505–533.
- Mendel, V., D. Sauter, C. Rommevaux-Jestin, P. Patriat, F. Lefebvre, and L. M. Parson (2003), Magmato-tectonic cyclicity at the ultra-slow spreading Southwest Indian Ridge: Evidence from variations of axial volcanic ridge morphology and abyssal hills pattern, *Geochem. Geophys. Geosyst.*, *4*(5), 9102, doi:10.1029/2002GC000417.
- Meyzen, C. M., M. J. Toplis, E. Humler, J. N. Ludden, and C. Mével (2003), A discontinuity in mantle composition beneath the Southwest Indian Ridge, *Nature*, *421*(6924), 731–733.
- Meyzen, C. M., J. N. Ludden, E. Humler, B. Luais, M. J. Toplis, C. Mével, and M. Storey (2005), New insights into the origin and distribution of the DUPAL isotope anomaly in the Indian Ocean mantle from MORB of the Southwest Indian Ridge, *Geochem. Geophys. Geosyst.*, *6*, Q11K11, doi:10.1029/2005GC000979.
- Michael, P. J., et al. (2003), Magmatic and amagmatic seafloor generation at the ultraslow-spreading Gakkel ridge, Arctic Ocean, *Nature*, *423*, 956–961.
- Miller, D. J., and N. I. Christensen (1997), Seismic velocities of lower crustal and upper mantle rocks from the slow-spreading mid-Atlantic ridge, south of the Kane Transform zone (MARK), *Proc. Ocean Drill. Program Sci. Results*, *153*, 437–454.
- Minshull, T. A., M. R. Muller, and R. S. White (2006), Crustal structure of the Southwest Indian Ridge at 66 degrees E: Seismic constraints, *Geophys. J. Int.*, *166*(1), 135–147.
- Muller, M. R., T. A. Minshull, and R. S. White (1999), Segmentation and melt supply at the Southwest Indian Ridge, *Geology*, *27*(10), 867–870.
- Natland, J. H. (1991), Indian ocean crust, in *Oceanic Basalts*, edited by P. A. Floyd, pp. 63–93, Blackie, Glasgow.
- Neumann, G. A., and D. W. Forsyth (1993), The paradox of the axial profile: Isostatic compensation along the axis of the Mid-Atlantic Ridge?, *J. Geophys. Res.*, *98*(B10), 17,891–17,910.
- Patriat, P., and J. Segoufin (1988), Reconstruction of the Central Indian Ocean, *Tectonophysics*, *155*, 211–234.
- Phipps Morgan, J., E. M. Parmentier, and J. Lin (1987), Mechanisms for the origin of Mid-Ocean Ridge axial topography: Implications for the thermal and mechanical structure of accreting plate boundaries, *J. Geophys. Res.*, *92*, 12,823–12,836.
- Price, R. C., A. K. Kennedy, M. Riggs-Sneeringer, and F. A. Frey (1986), Geochemistry of basalts from the Indian Ocean Triple Junction: Implications for the generation and evolution of Indian Ocean Ridge basalts, *Earth Planet. Sci. Lett.*, *78*, 379–396.
- Reid, I., and H. R. Jackson (1981), Oceanic spreading rate and crustal thickness, *Mar. Geophys. Res.*, *5*, 165–172.
- Robinson, C. J., R. S. White, M. J. Bickle, and T. A. Minshull (1996), Restricted melting under the very slow-spreading Southwest Indian Ridge, in *Tectonic, Magmatic, Hydrothermal and Biological Segmentation of Mid-Ocean Ridges*, edited by C. J. MacLeod, P. A. Tyler, and C. L. Walker, *Geol. Soc. Spec. Publ.*, *118*, 131–141.
- Robinson, C. J., M. J. Bickle, T. Minshull, R. S. White, and A. R. L. Nichols (2001), Low degree melting under the Southwest Indian Ridge: The roles of mantle temperature, conductive cooling, and wet melting, *Earth Planet. Sci. Lett.*, *188*, 383–398.
- Rommevaux-Jestin, C., C. Deplus, and P. Patriat (1997), Mantle Bouguer anomaly along an ultra-slow spreading ridge: Implications for accretionary processes and comparison with results from Central Mid-Atlantic Ridge, *Mar. Geophys. Res.*, *19*, 481–503.
- Rubin, A. M. (1995), Propagation of magma-filled cracks, *Annu. Rev. Earth Planet. Sci.*, *23*, 287–336.
- Sauter, D., P. Patriat, C. Rommevaux-Jestin, M. Cannat, A. Briais, and Gallieni Shipboard Scientific Party (2001), The Southwest Indian Ridge between 49°15'E and 57°E: Focused accretion and magma redistribution, *Earth Planet. Sci. Lett.*, *192*, 303–317.
- Sauter, D., L. M. Parson, V. Mendel, C. Rommevaux-Jestin, O. Gomez, A. Briais, C. Mével, K. Tamaki, and Fuji Scientific Team (2002), TOBI sidescan sonar imagery of the very slow-spreading Southwest Indian Ridge: Evidence for along-axis magma distribution, *Earth Planet. Sci. Lett.*, *199*, 81–95.
- Schiano, P., J. L. Birck, and C. Allegre (1997), Osmium-strontium-neodymium-lead isotopic covariations in mid-ocean ridge basalt glasses and the heterogeneity of the upper mantle, *Earth Planet. Sci. Lett.*, *150*, 363–379.
- Scott, D. R. (1992), Small-scale convection and mantle melting beneath mid-ocean ridges, in *Mantle Flow and Melt Generation at Mid-Ocean Ridges*, *Geophys. Monogr. Ser.*, vol. 71, edited by J. Phipps Morgan, D. K. Blackman, and J. M. Sinton, pp. 311–326, AGU, Washington, D. C.
- Seyler, M., M. Cannat, and C. Mével (2003), Evidence for major-element heterogeneity in the mantle source of abyssal peridotites from the Southwest Indian Ridge (52° to 68°E), *Geochem. Geophys. Geosyst.*, *4*(2), 9101, doi:10.1029/2002GC000305.
- Sleep, N. H. (1975), Formation of oceanic crust: Some thermal constraints, *J. Geophys. Res.*, *80*(29), 4037–4042.
- Small, C. (1998), Global systematics of mid-ocean ridge morphology, in *Faulting and Magmatism at Mid-Ocean Ridges*, *Geophys. Monogr. Ser.*, vol. 106, edited by W. R. Buck, et al., pp. 1–25, AGU, Washington, D. C.
- Smith, D. K., and J. R. Cann (1999), Constructing the upper crust of the Mid-Atlantic Ridge: A reinterpretation based on the Puna Ridge, Kilauea volcano, *J. Geophys. Res.*, *104*(B11), 25,379–25,399.
- Smith, W. H., and D. T. Sandwell (1997), Global seafloor topography from satellite altimetry and ship depth soundings, *Science*, *277*, 1956–1962.
- Sotin, C., and E. M. Parmentier (1989), Dynamical consequences of compositional and thermal density stratification beneath spreading centers, *Geophys. Res. Lett.*, *16*(8), 835–838.
- Spiegelman, M., and D. McKenzie (1987), Simple 2-D models for melt extraction at midocean ridges and island arcs, *Earth Planet. Sci. Lett.*, *83*(1–4), 137–152.
- Standish, J. J., H. J. B. Dick, A. P. le Roex, W. G. Melson, and T. O'Hearn (2002), Major and trace element geochemistry: Ultra-slow spreading SWIR (9°–25°E), *Eos Trans. AGU*, Fall Meet. Suppl., 83(47), T11A-1233.



- Standish, J. J., H. J. B. Dick, S. R. Hart, M. D. Kurz, P. J. Michael, and F. Frey (2006), Chemical variations and MORB generation on the ultraslow-spreading Southwest Indian Ridge (9°–25°E), *Eos Trans. AGU*, Fall Meet. Suppl., 87(52), Abstract V11G-05.
- Su, Y. S. (2002), Mid-ocean ridge basalts trace element systematics: Constraint from data base management, ICP-MS analyses, global data compilation, and petrologic modeling, Ph.D. thesis, Columbia Univ., New York.
- Tryggvason, E. (1994), Surface deformation at the Krafla Volcano, North Iceland, 1982–1992, *Bull. Volcanol.*, 56(2), 98–107.
- Tucholke, B. E., J. Lin, and M. C. Kleinrock (1998), Megamullions and mullion structure defining oceanic metamorphic core complexes on the Mid-Atlantic Ridge, *J. Geophys. Res.*, 103(B5), 9857–9866.
- Weissel, J. K., and G. D. Karner (1989), Flexural uplift of rift flanks due to mechanical unloading of the lithosphere during extension, *J. Geophys. Res.*, 94(B10), 13,919–13,950.
- Wessel, P., and W. H. F. Smith (1995), New version of the Generic Mapping Tools released, *Eos Trans. AGU*, 76, 329.
- White, R. S., D. McKenzie, and R. K. O’Nions (1992), Oceanic crustal thickness from seismic measurements and rare earth element inversions, *J. Geophys. Res.*, 97(B13), 19,683–19,715.
- White, R. S., T. A. Minshull, M. J. Bickle, and C. J. Robinson (2001), Melt generation at very slow-spreading oceanic ridges: Constraints from geochemical and geophysical data, *J. Petrol.*, 42(6), 1171–1196.
- Wright, T. J., C. Ebinger, J. Biggs, A. Ayele, G. Yirgu, D. Keir, and A. Stork (2006), Magma-maintained rift segmentation at continental rupture in the 2005 Afar dyking episode, *Nature*, 442(7100), 291–294.